Summer 2020

Development of a CVD Assisted PLD System for Growing Novel Materials

Sinjan Majumder
Missouri State University, Sinjan1994@live.missouristate.edu

DEVELOPMENT OF A CVD ASSISTED PLD SYSTEM FOR GROWING NOVEL MATERIALS

A Master's Thesis

Presented to

The Graduate College of

Missouri State University

In Partial Fulfillment

Of the Requirements for the Degree

Master of Science, Materials Science

By

Sinjan Majumder

August 2020

DEVELOPMENT OF A CVD ASSISTED PLD SYSTEM FOR GROWING NOVEL MATERIALS

Physics Astronomy and Materials Science

Missouri State University, August 2020

Master of Science

Sinjan Majumder

ABSTRACT

The fundamental step for development of novel materials like semiconductors involves stacking of layers of thin films of materials with desired properties on a particular substrate. In order to study the properties of these materials for research purposes in the laboratory, development of a clean fabrication technique is essential. PLD is a technique employed for growing thin films using laser ablation of a target material. CVD is an alternate method used to deposit solid materials from a gaseous phase. However, combining these two techniques can enhance plume, gas and laser interaction to facilitate the growth of novel materials with new and improved properties. Conformity and purity play pivotal roles in the thin film growth process. While working under Ultra-high vacuum can eliminate impurities, on the other hand, proper screening and thermal activation of the plasma of ablated materials ensures a smooth registration of the film with the substrate. We aim at studying the effect of substrate, temperature and carrier gas on the resulting films and to allow variance between the two techniques. For analysis and characterization of the developed film, we employ standard techniques like SEM, XRD, AFM, Raman spectroscopy and Profilometry. For initial proof of performance, we demonstrate growing a metal nitride.

KEYWORDS: ultra-high vacuum, PLD, CVD, optical chopper, conformity, purity, novel materials, thin film, aluminum nitride, 2D materials

DEVELOPMENT OF A CVD ASSISTED PLD SYSTEM FOR GROWING NOVEL MATERIALS

By

Sinjan Majumder

A Master's Thesis
Submitted to the Graduate College
Of Missouri State University
In Partial Fulfillment of the Requirements
For the Degree of Master of Science, Materials Science

August 2020

Approved:

David Cornelison, Ph.D., Thesis Committee Chair

Kartik Ghosh, Ph.D., Committee Member

Ridwan Sakidja, Ph.D., Committee Member

Julie Masterson, Ph.D., Dean of the Graduate College

ACKNOWLEDGEMENTS

Foremost, I am grateful to my advisor, Dr. David Cornelison for giving me the opportunity to work on this exciting project. These two years has been a great learning curve full of challenges and his constant support, guidance and inspiration throughout this journey is invaluable. Without his enthusiasm and ideas, this project would not have been possible. I would like to thank Dr. Kartik Ghosh for helping me stay focused and motivated throughout my graduate studies. It was great comfort in knowing that I could always use his insightful inputs regarding my research, studies or life in general. My sincere thanks to Dr. Ridwan Sakidja for taking time out of his busy schedule to help me whenever I approached him with a research problem and his constructive feedback on the same. Special thanks to Rishi Patel of Jordan Valley Innovation Centre for his help. I would like to mention Department Head, Dr. Robert Mayanovic for his endless cooperation and allowing me to use the facilities of the department whenever I needed them.

I truly value the help and assistance of Nick Rogers, Christian Oldham and Raven Quick during my experiments. I would also like to acknowledge the efforts of Brian Grindstaff for machining and designing various components I have used in this project. I take this opportunity to thank all other faculty members, staff and my colleagues for their support throughout my time spent at Missouri State.

Last but not the least, I am indebted to my parents, Prithwi Ranjan Majumder and Krishna Majumder for their endless sacrifices and sharing my dreams and aspirations with me. I proudly dedicate this thesis to them.

TABLE OF CONTENTS

LIST OF TABLES

LIST OF FIGURES

INTRODUCTION

1.1 Motivation

Today, we are standing at a juncture where our world is advancing at a rapid pace and changing on a daily basis. We have just started on our rollercoaster ride to innovations that will pave our way to a smarter and better future. From a materials perspective, one particular area which has attracted significant interest and grown by leaps and bounds is that of thin films. So far, it has touched on every sphere of our life-ranging from healthcare, utilities, industry, electronic devices to even defense and energy sectors. In order to broaden our spectrum, we have transferred our gaze to the nano scale which has opened new possibilities unimagined in the past. However, this has brought us face to face with new challenges as we try to push our limits.

The present day materials industry is driven by the requirement for advanced processing tools for fabricating devices with improved performance but at a reduced cost. Since the film quality is correlated with the number of defects, particulate contamination originating from the processing cycle needs to be addressed appropriately. [1-2] Over the years, a number of vacuum deposition techniques like Pulsed Laser Deposition (PLD), Thermal Evaporation, Sputtering, Chemical Vapor Deposition and Molecular Beam Epitaxy have been developed for the fabrication of thin films. Some of these tools like PLD for example, is extremely versatile and used for growing different materials like Transition Metal Oxides (TMO), organic materials and Transition Metal Di-chalcogenides (TMDs). However, the major demerits of such a tool are probably deposition of nodules and lack of throughput. Thus, in order to grow novel materials like epitaxial films, it is vital to have a deposition chamber designated to a particular film type. Our primary goal is to combine the merits of two distinct deposition techniques and construct a

clean deposition system in our department that is free from contamination and can be used for the low-cost fabrication of novel materials.

1.2 Role of Ultra-High Vacuum (UHV) in Controlling Contamination

As pointed out in the previous section, a primary concern that needs to be addressed before working with thin films geared towards devices is cleanliness of the deposition chamber. Presence of unwanted impurities in the growth environment can prove to be detrimental to the fabrication process and may even alter the characteristics of the film which is undesirable. Further, rogue particles even in trace amounts, can introduce a fair amount of uncertainty in the analysis and characterization process post deposition. Hence, it is in the best interest of thin film engineers to ensure that these issues are eliminated to the best of ability during the early stages of the experimental process. Thus, the starting pressure is highly critical to the end results obtained on the films grown. Most vacuum systems can be classified into one of the following categories shown in Table 1.1 based on their range of pressure. Out of these, ultra-high vacuum is the most preferred region of operation for a number of reasons like molecular density, mean free path of the molecules and time taken for the formation of a monolayer of contamination on the surface of the film. [3]

Molecular density is defined as the number of molecules per unit volume. Assuming ideal gas behavior inside the chamber, the formula for the molecular density can be derived from the gas equation

$$PV = nRT = nkN_AT \qquad (1)$$

where P = pressure, V= volume, n =moles, k = Boltzmann's constant, N_A = Avogadro's number and T = temperature in absolute scale. The above formula can be rearranged to show that

$$\frac{n}{V} * N_A = \frac{P}{kT} = N \text{ (molecular density)} \qquad (2)$$

Thus, the number of molecules per unit volume, i.e., molecular density is directly related to the

Table 1.1 Classification of vacuum based on pressure range [4]

Pressure Range	Pressure (mbar)	Molecules per cm^3
Low vacuum	10^3 to 10	$2.65 * 10^{19}$ - $2.65*10^{16}$
Medium vacuum	10 to 10^{-5}	$2.65 * 10^{16}$ - $2.65 * 10^{13}$
High vacuum	10^{-5} to 10^{-7}	$2.65 * 10^{13}$ - $2.65 * 10^{9}$
Ultra-high vacuum	10^{-7} to 10^{-12}	$2.65 *10^{9}$ - $2.65 * 10^{4}$

pressure inside the chamber and inversely related to the temperature inside the chamber. Thus, a chamber having a low molecular density is more likely to be free from contamination. Working in the high-vacuum to ultra-high vacuum range of pressures partially resolves issues related to purity of the chamber.

The next important factor to be considered is the mean free path of the molecules inside the chamber. According to the kinetic theory model, gas molecules are in a state of continuous random motion. The kinetic energy of these molecules are directly proportional to their absolute temperature. During this spontaneous motion, these molecules often take arbitrary trajectories and undergo collisions with one another. The average path length traversed by each molecule before undergoing a subsequent collision is defined as their "mean free path". Mathematically, the expression for mean free path is formulated as:

$$\lambda = \frac{kT}{\sqrt{2}Pd^2} \qquad (3)$$

where k = Boltzmann's constant, T= absolute temperature, d= diameter of the colliding gas molecules and P= chamber pressure. The above formula further helps explaining the fact that a large number of particles correspond to a shorter mean free path. This is due to an increased frequency of collisions between the particles. In the high vacuum range, the mean free path of the gas molecules is very large. This means that the interaction of the gas molecules in the molecular beam with the ambient gases in the chamber is reduced to a minimum. The primary point to starting with good vaccum is to reduce contamination from unintended sources. Also, any characteristic change in the properties of the substrate can be associated solely with its interplay with the plume and the process gas. As illustrated by the Table 1.2 below, we can observe the change in mean free path of a particular gas molecule as function of the vacuum

Table 1.2 Mean free path of Nitrogen gas at 273 kelvin [5]

Pressure (torr)	Mean free path (m)
$7.5 * 10^{-4}$	$5.9 * 10^{-2}$
$7.5 * 10^{-5}$	$5.9 * 10^{-1}$
$7.5 * 10^{-6}$	$5.9 * 10^{0}$
$7.5 * 10^{-7}$	$5.9 * 10^{1}$
$7.5 * 10^{-8}$	$5.9 * 10^{2}$
$7.5 * 10^{-9}$	$5.9 * 10^{3}$
$7.5 * 10^{-9}$	$5.9 * 10^{4}$

chamber pressure. In accordance with the formula above, the mean free path increases significantly at high vacuum range when compared against its value at atmospheric pressure. Elevated temperatures could further extend the path length when the vacuum pressure is held constant. Thus, a combination of good vacuum and temperature provides favorable conditions for thin film growth.

However, the most crucial of all factors is the time taken to form a monolayer of contamination as a function of chamber pressure. In vacuum engineering, the amount of adsorbed gas on a particular surface is expressed in terms of monolayers. In an article published by CERN, Geneva, Mathewson shows by elementary calculation that a monolayer of contaminant in a cubic litre volume can cause a pressure increment of about $1.7*10^{-2}$ torr. [6] The advantage of an Ultra-High vacuum system over High Vacuum system in terms of controlling contamination is further illustrated in Figure 1.1. Thus, efficient vacuum engineering must be focused on removing adsorbed residual gas on surfaces.

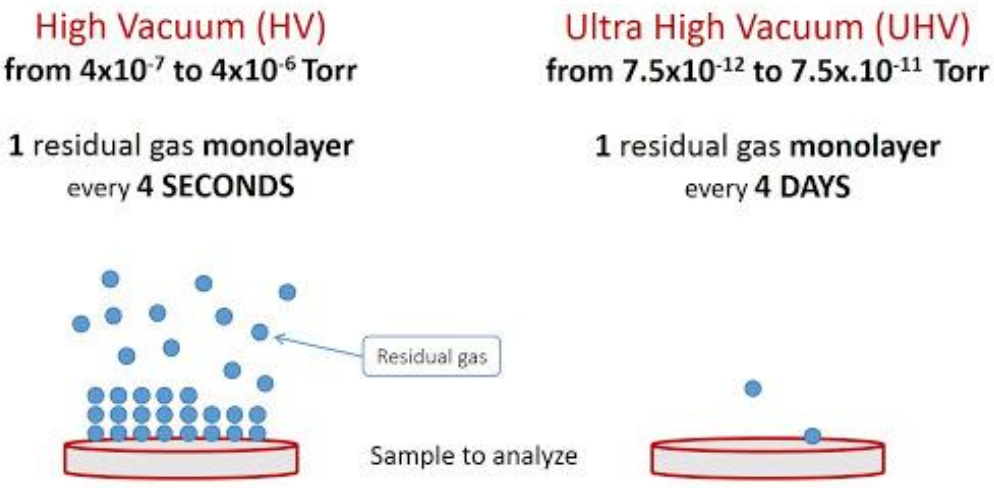

Figure 1.1. Time taken to form a monolayer as a function of chamber pressure [7]

So far, we have addressed contamination issues based on chamber pressure. In the next segment, we try to identify and discuss the source of particle impurities in two commonly used deposition systems and evaluate their individual merits and demerits.

1.3 Pulsed Laser Deposition

The discovery of excimer lasers led to the inception of a new thin film deposition technique called Pulsed Laser Deposition (PLD). Over the past few decades, PLD has been extensively used for the deposition of a diverse range of materials spanning metals, ceramics, optoelectronic materials, biomaterials, superconductors and semiconductors. [8-12] The conceptual simplicity and relative straightforwardness of experimental procedure has led to the large scale adoption of this physical vapor deposition technique as a growing tool.

In a typical PLD chamber, shown in Figure 1.2, a high energy pulsed UV laser beam is directed on the surface of a target material that is to be deposited. The incident energy of the incoming pulse is used to melt and vaporize a portion of the surface by a process called "ablation". This rapid heating creates a plasma of ablated materials that includes atoms, ions, molecules, electrons and particulate clusters commonly termed as the "plume". This plume

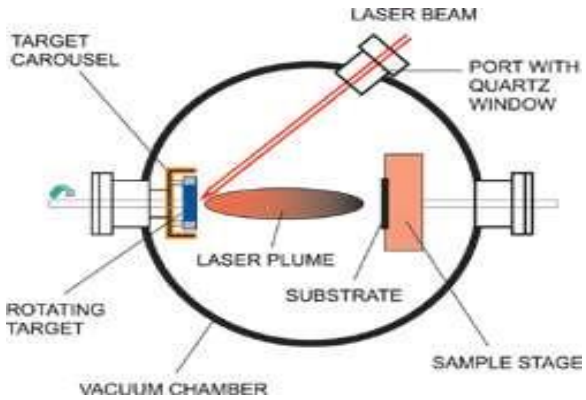

Figure 1.2. Schematic of a typical PLD chamber used for growing thin films [13]

accelerates away from the target and is collected by a substrate where it condenses to form a film.

Apart from the relative ease of operation, PLD has several advantages compared to other techniques. [14] Firstly, it allows reasonable control over the deposition rate by adjusting only a limited set of parameters like the laser fluence and number of pulses. This in turn allows controllability over film thickness. Secondly, during the ablation process, a stoichiometric transfer of material from a complex target onto a substrate can be achieved. This makes it possible to grow multi-component materials like ceramic oxides and compound semiconductors. In the presence of certain ambient gases like oxygen, a reactive deposition can be carried out where the ablated particles react chemically with the gas before forming a film. Lastly, a variety of hetero-structured uniform thin films can be grown by stacking individual layers having distinct compositions. The film uniformity can be explained by the forward directionality of the plume covering a shallow angle as illustrated in Figure 1.3.

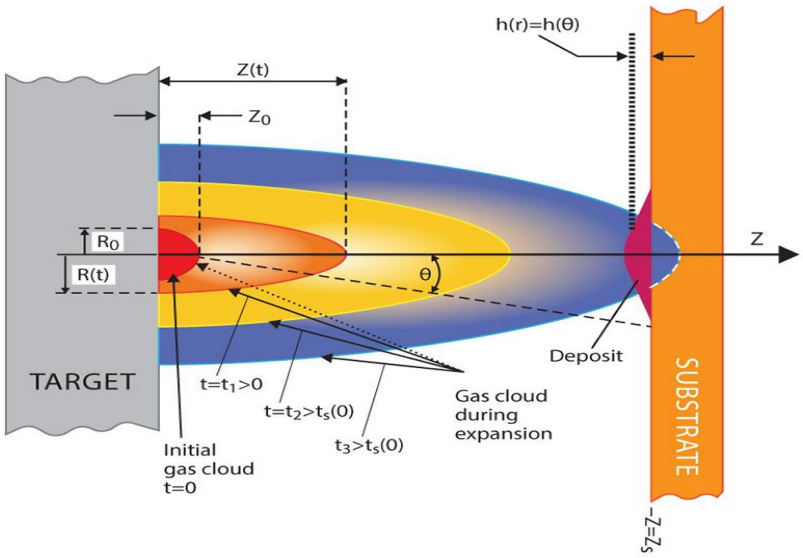

Figure 1.3. Schematic for the vapor cloud expansion in PLD after target irradiation [15]

However, despite these distinguishable characteristics, PLD has some disadvantages which make it unsuitable for large scale manufacturing. [16] The biggest challenge is the presence of micron-sized particles and clusters in the plume that can affect the film quality. The fabrication of devices like semiconductor chips often involves patterning intricate features having dimensions in the range of nanometers. The ejection of such particles may degrade the film quality making it less than suitable for these sophisticated applications. The underlying complex mechanism behind the plume generation often leads to different velocity profiles for the individual elements. In such cases, the introduction of background gases become necessary to avoid film abnormalities resulting from this differential expansion. Furthermore, the inhomogeneous energy distribution in the plume and its narrow forward peak leads to low coverage restricting growth on bigger substrates. Thus, despite being an adaptable and resourceful technique, certain enhancements need to be incorporated before high quality films can be grown using PLD.

1.4 Chemical Vapor Deposition

Chemical Vapor Deposition (CVD) is a growing technique where a gaseous precursor mixture is flown into a vacuum chamber and eventually allowed to be deposited as a solid layer on a heated substrate upon coming in contact with it. Figure 1.4 illustrates the basic operation of a CVD chamber. Usually, a convection technique is used to drive the gases into the reaction chamber. The precursor gases adhere to the substrate and react chemically on its surface to form the film. In most cases there is an energy source that initiates the reaction, i.e. hot wire, plasma assisted CVD, etc. The by-products if any, are eliminated through the exhausted vent. CVD is widely used for optoelectronic applications, various coatings and in the semiconductor industry.

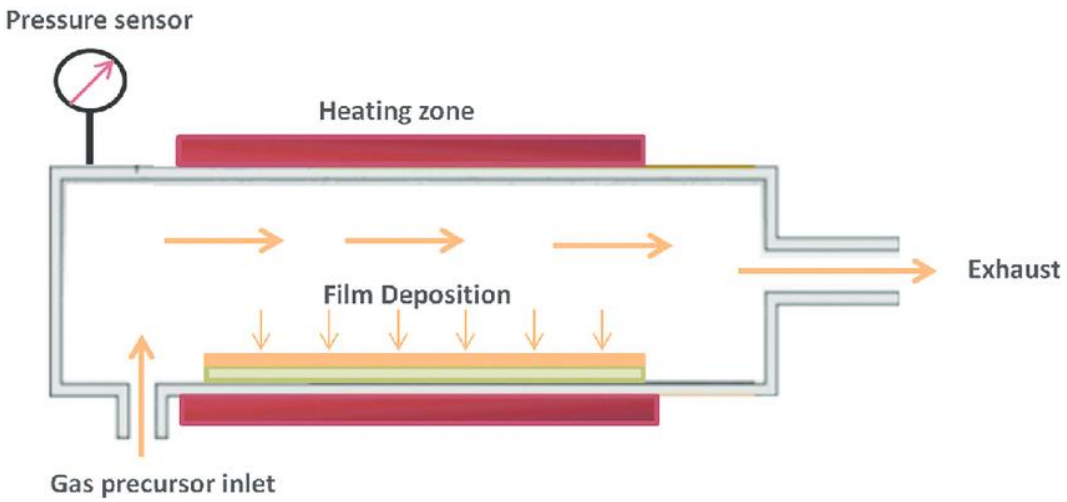

Figure 1.4. Schematic representation of the CVD process [17]

This technique has a few distinct advantages when compared against competing physical vapor deposition methods. The composition of the precursor gases can be easily altered to get the desired reaction in order to deposit a particular film. As shown in Figure 1.5, the precursor gases, once bled in, occupy the entire chamber volume and do not have any restrictions for coming to

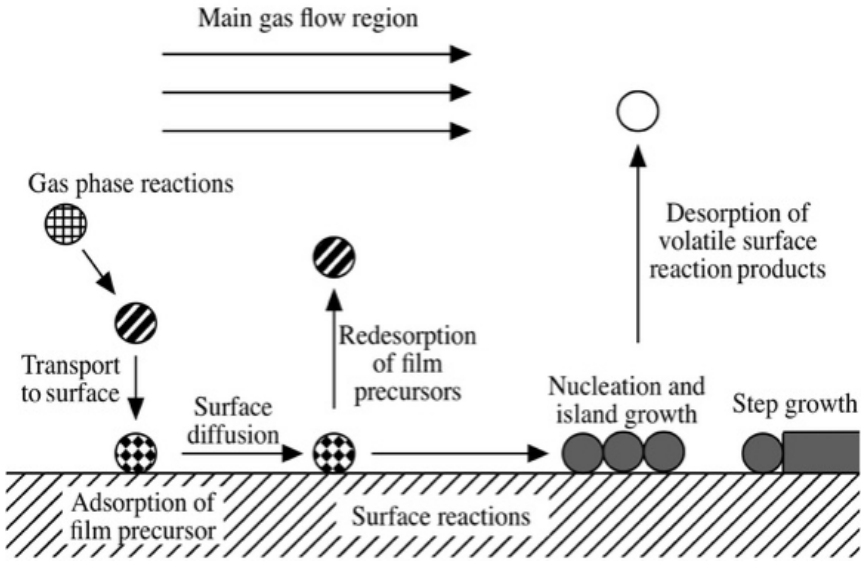

Figure 1.5. Surface reaction mechanism in Chemical Vapor Deposition [18]

contact with the substrate. This is advantageous for coating irregular surfaces or complicated structures in devices like gates and interconnects for transistors. This is different from PVD techniques like PLD where the plume is highly directional and only reach the substrate at specific narrow angles. Thus, the throughput and the deposition rates are significantly higher in CVD. This makes this process more practical and economically feasible for high volume manufacturing. Further, the stoichiometry of the as-grown films can easily be adjusted by regulating the concentrations of the precursor gases. Also, since the reaction takes place on the surface of the substrate, the film is bonded strongly to it and is resistant to mechanical strains. Due to the cumulative effect of these factors, CVD can be used to grow films that demonstrate high quality and purity. Figure 1.6 shows a comparative study between defects generated by CVD and PVD processes and categorizes them according to particle size. It can be further inferred that the number of defect clusters generated through CVD are notably less making it a reliable process.

Defect type	CVD-coating	PVD-coating
Particles $0.2\,\mu m < d < 3\,\mu m$	–	$(4000 \pm 900) \cdot 10^2/mm^2$
Particles $3\,\mu m < d$	$28 \pm 5/mm^2$	$(2 \pm 0.5)\ 10^2/mm^2$
Craters $0.2\,\mu m < d < 3\,\mu m$	–	$(500 \pm 30) \cdot 10^2/mm^2$
Craters $> 3\,\mu m$	–	$(2 \pm 0.5) \cdot 10^2/mm^2$

Figure 1.6. Defect comparison between CVD and PVD coating based on particle size [19]

Nevertheless, a major drawback of the CVD process is the potential requirement of high substrate temperatures for reaction. [20] This limits the choice of substrates that can be used for growing a desired film. Another issue is the frequent generation of toxic waste gases during the

reaction. [21] Additional safety measures are required and proper waste handling must be ensured in order to prevent accidents like leakage or explosion. Thus, despite being a cleaner and much more efficient technology, CVD raises different concerns and imposes its own constraints on the variety of materials that can be fabricated.

1.5 Compound Deposition Techniques for Addressing Deposition Challenges

The discussions in the previous section underscores the challenges associated with PLD and CVD. Over the past few decades, scientists and researchers across the globe have tried to formulate suitable modifications to these processes in order to make them more robust and efficient. Such concerted efforts have led to the innovation of a number of compound deposition techniques that have attracted much attention for their effectuality in addressing these fabrication bottlenecks.

In PLD for example, mechanical velocity filters in the form of shutters have been used and tested to prevent micro droplets in the plume from reaching the substrate. [22] The filters consist of a rotating vane and only those particles whose linear velocity match the rotational speed of the shutter are allowed to pass through. An alternate way to screen particulates is the use of off-axis geometry for deposition. In this particular arrangement, the normals to the surface of the target and the substrate are perpendicular to each other. [23] Since majority of the droplets approach the substrate perpendicularly, this anti-parallel geometry serves to block their transport to the substrate. Gyorgy et al. [24] suggested a mechanism involving the usage of two synchronized laser pulses for depositing particulate free thin films. One of the laser beams approaching the target perpendicularly is responsible for creating the ablation plume while a secondary beam running parallel to it is used for washing away droplets. Similarly, several enhancements to the

mainstream CVD technique have been widely accepted and are standard processes for specific applications today. Laser assisted CVD (LACVD), a popular variant, has been extensively used for growing metal nitrides, carbides as well as carbon nanotubes. [25] Figure 1.7 shows a typical set up for LACVD and illustrates the fundamental process leading to the film growth. In this approach, the substrate is irradiated with a focused laser beam in order to

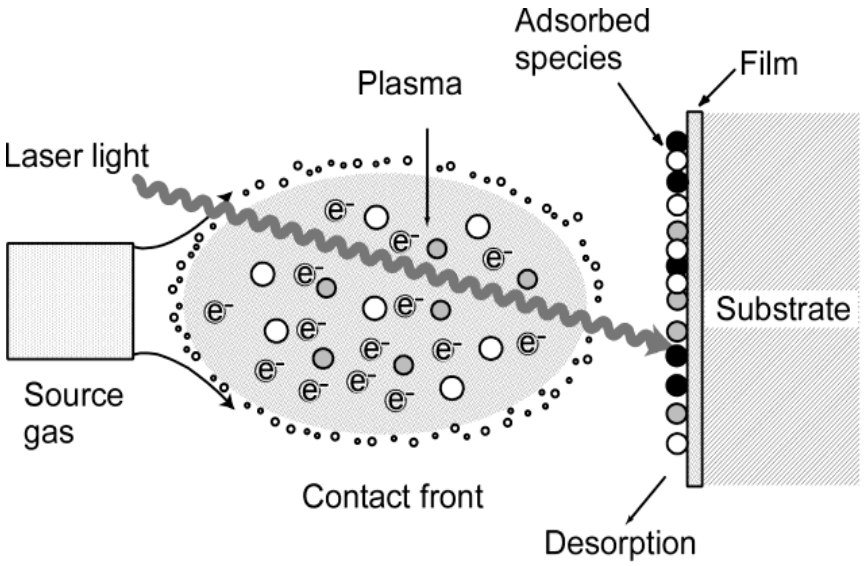

Figure 1.7. Schematic representation of reaction mechanism in LACVD [26]

aid the reaction taking place on its surface. This process can be further extended to precursors gases that undergo UV photo-catalytic decomposition. In such scenarios, this arrangement is appropriately denominated as "Photo-assisted CVD". [27] The convenience of using this routine is that the energy of the photons can be well utilized and hence, depositions can be carried out at much lower temperatures. This gives it an edge over thermal CVD by circumventing the need for high substrate temperatures. RF Plasma-Assisted CVD schematically represented in Figure 1.8 uses an electrical energy source to create a plasma stream containing ions and free electrons.

This energy is rapidly transferred to the precursor gases enabling free radical formation and thereby activating reaction. This in turn activates the reaction in the precursor gases Boyd et al. [28] introduced a new process called plasmon-assisted CVD (PCVD) where he uses plasmon resonance as a local heat source for decomposing the precursor gases and initiating chemical reaction only at targeted regions on the surface of the substrate. Thus, it allows great selectivity and unnecessary coating of the entire substrate can be avoided. In addition to the above mentioned techniques, microwave plasma-assisted CVD and hot filament CVD are other nuanced versions that are in practice today. Comprehensive analysis of the aforementioned

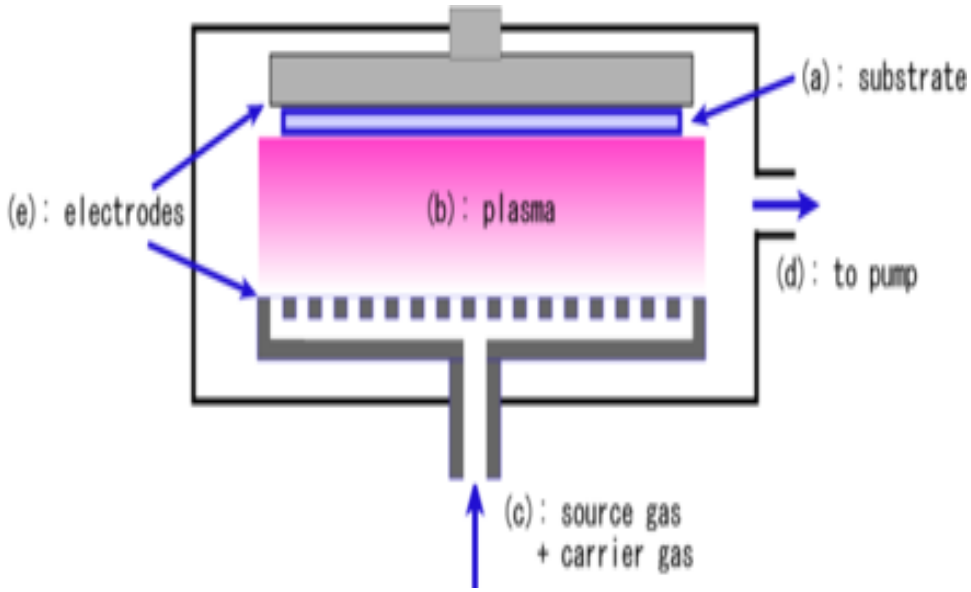

Figure 1.8. Schematic representation of RF Plasma-Assisted CVD process [29]

processes reveal an iterative theme of amalgamating two or more sub-processes and encapsulating them into a single deposition technique for superior performance of the overall system. Such systems are commercially available and can be acquired from the market according to desired specification needs. However, despite having pronounced benefits, a major drawback

of these commercial units is that they are often expensive, making them unfeasible for routine laboratory research. As an alternative, such a system can be custom built in the laboratory with competing performance but at a much lower cost. In this project, we make an endeavor to assemble a CVD assisted PLD system of our own and optimize it for growing contamination free epitaxial quality films. For initial purposes, we chose to fabricate nitride films because they are relatively cleaner than other materials in terms of adsorbing on the chamber walls and hence, does not limit future growth of other materials with the same chamber. We further demonstrate that the developed system is tested and capable of but not limited to the growth of nitrides.

EXPERIMENTAL

2.1 Design and Engineering

2.1.1 General construction. The custom built UHV chamber shown in the Figure 2.1 below was designed and constructed by our research group at MSU. The fundamental components of our system includes an ion pump, a gate valve, a turbo pump and a rotary pump for pressure control purposes. The sensor network comprises of an ionization, thermocouple gauge, baratron gauge and a thermistor gauge. Using a combination of the above array of sensors and transducers, we are able to monitor the chamber pressure, temperature and the flow rates of process gas into the chamber. For gas handling purposes, we use a manifold valve and a leak valve for introducing either individual gases or a mixture of them. A closed gas cabinet which is connected to the fume hood is used to secure gas bottles, especially hazardous ones. For growing purposes we use a solid state Nd:Yag Laser having a wavelength of 266nm which serve as the source of pulsed laser beam for film deposition. The geometry and path traversed by the laser beam is controlled by using a combination of beam splitter, mirrors, lenses and choppers. At the very top of our chamber, is the sample holder assembly. The chamber has view ports and windows placed at strategic locations. Each one of these either serve as entrances for the laser beam or offer a view to the inside parts of the chamber during deposition. The view ports are made of glass while the windows are made of quartz. In general, the entire chamber was constructed with stainless steel segments, flanges and tubing to ensure consistency and minimize degassing of the internal parts of the chamber while under vacuum conditions. The details of the working of individual components is discussed in the subsequent sections.

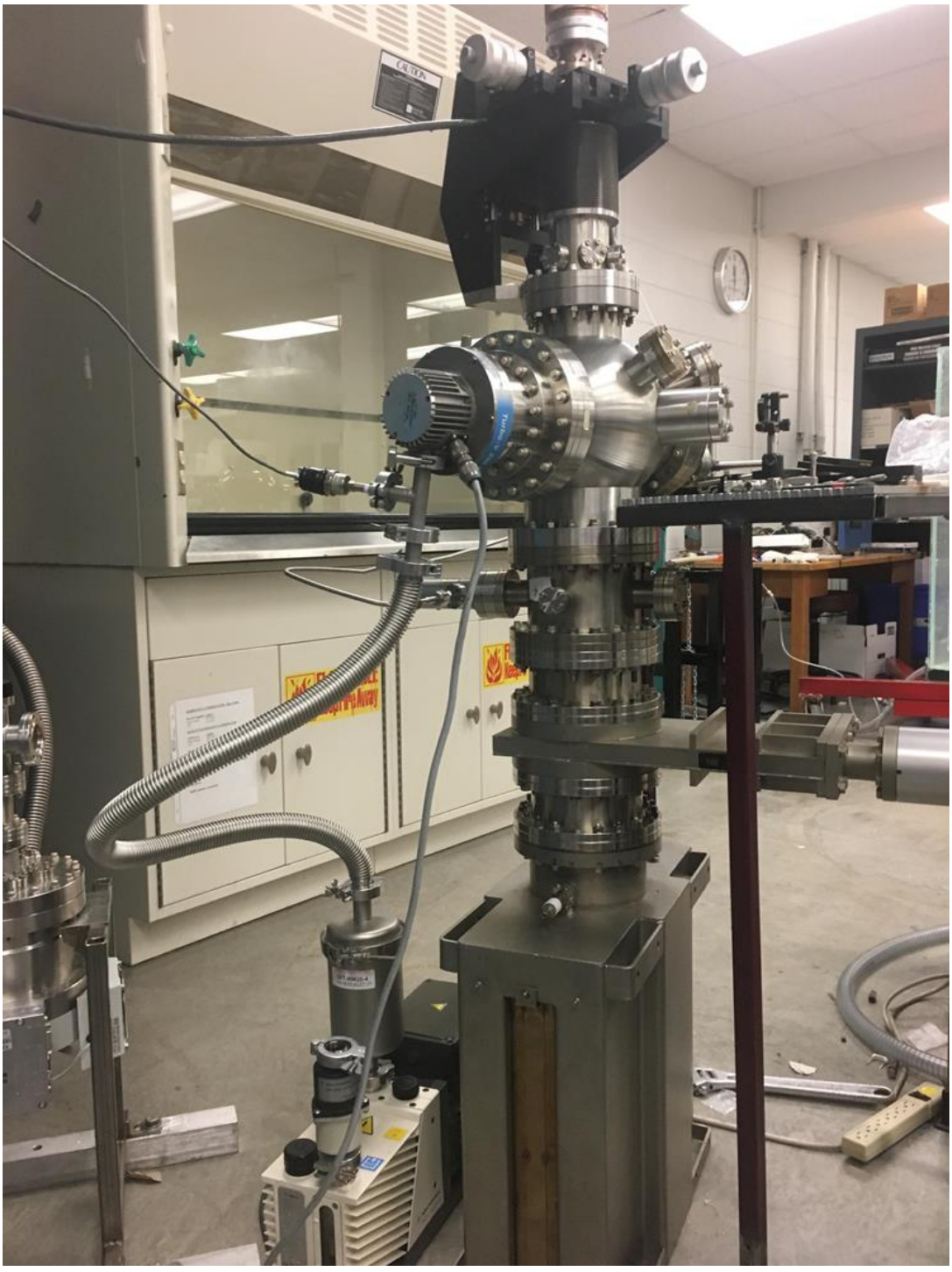

Figure 2.1. Overall construction of the CVD assisted PLD system

2.1.2 Pumping assembly. The effective volume of the chamber to be used for pumping was isolated from the rest of the unit using a gate valve. Although not used in our current experiments, an ion pump is placed below the gate valve. This was done in order to make the system capable of attaining UHV pressures which is desired in the future stages. To begin the initial pump down of the chamber we use a standard direct drive rotary vacuum pump. This rotary pump allows the chamber to be pumped down to low vacuum, typically around $50*10^{-3}$ torr. A thermocouple gauge mounted on a T-section is mounted on the downstream pipeline of the turbo. This thermocouple gauge is connected to a meter which indicates the roughing pressure. This rotary pump backs up the turbo pump and sets the conditions before the latter can be functional. In most typical conditions, the rotary pump can yield pressures in low vacuum range after about twenty minutes of operation.

The heart of the chamber is connected to a turbo molecular pump. At normal operation, the turbo pump can reach rotational speeds of 56 KRPM at steady state. Depending on the environmental conditions and the duration of pumping, our chamber demonstrated a maximum low pressure of about 10^{-9} torr. When the humidity in the air is higher, it takes a longer amount of time to pump down the chamber to the same pressure. This is due to the large amount of water vapor trapped in the walls of the chamber which starts outgassing in vacuum. Although the above problem could be resolved by a thorough bakeout procedure of the walls of the chamber between every subsequent experimental runs, we did not perform it. This was done partly in order to save valuable time and also because satisfactory levels of vacuum pressures could be attained without the rigorous procedure. A butterfly throttle valve is fitted between the flanges of the turbo pump and the main chamber. This allows controllability of the exposure of the blades of the turbo to the gas molecules. For example, when a high amount of ambient gases is

introduced, the throttle valve can be partially closed, so that only a small amount of gas molecules hit the blades of the turbo. This serves a dual purpose. Firstly, it reduces friction in the turbo blades and prevents overheating. Secondly, it proves to be advantageous by using less amount of gas to reach the same ambient pressures (due to the turbo being partially blocked). In addition to this arrangement, the turbo pump controller has an inbuilt feature that allows the rotational speed of the pump to be adjusted as desired. This mode of operation is called the standby mode and typically the rotation speed is set at 50% of the maximum operation speed. Thus, using a combination of the throttle valve and the standby feature we are able to use the turbo pump more efficiently while operating at higher ambient pressures needed for CVD experiments.

Special care is taken in regards to choice of pressure gauge depending on the pressure inside the chamber. As pointed out earlier, we use a thermocouple gauge to measure the roughing pressure. The ionization gauge is used in the pressure range of 10^{-5} to 10^{-9} torr. If the ionization gauge is operated above 10^{-4} torr, it can lead to the damage of the filaments and collector of the gauge. After the chamber has been pumped down to its base pressure, we introduce process gas into our system. The final pressure due to background gas in our system further dictates the choice of instrument for reading the pressure. For example, if the final pressure for film growth in the presence of process gas is 10^{-3} torr range, a switch must be made from the ionization gauge to the thermistor gauge before any gas is introduced. At any stage of the experiment, if a lower gas pressure or vacuum annealing is desired, then the ionization gauge can be switched back on accordingly.

2.1.3 Sample manipulator and target holder assembly. Before deposition can be carried out, a primary requirement is to have a holder to secure the target material to be ablated

and a sample stage that contains the substrate on which deposition takes place. We custom designed and built a new assembly specifically for this chamber at our facility in MSU**.** The final design was achieved after several rounds of rigorous testing including refinements in each phase. The sample holder consists of two pieces, i.e. a supporting base piece and a detachable sample manipulator used for mounting the substrate as shown in the Figure 2.2 (a) and (b) below. The base piece connects to a central axis that has a turnable screw head attached to it on the exterior of the chamber as shown in Figure 2.3. The sample holder in conjunction with the rotatable screw head forms the sample manipulator. This allows the sample to be manipulated azimuthally with three linear as well as rotational degrees of freedom.

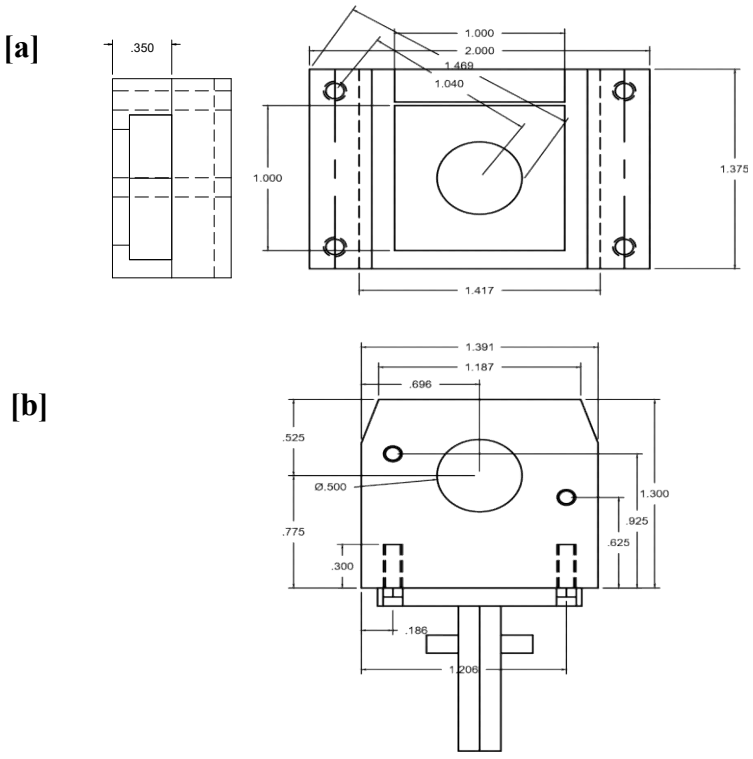

Figure 2.2. Top view of (a) base piece of sample holder and (b) detachable sample manipulator

.

Figure 2.3. Side view of sample manipulator assembly

The target holder assembly is shown in Figures 2.4 and 2.5 below. The arrangement is somewhat similar to the sample holder. However, the turnable screw head of the target holder is the only adjustable element from the exterior of the chamber. In order to add flexibilty to the target in the X-Y plane, a slight adjustment was made in the design. Instead of connecting the seat of the target directly to the central axis of the holder, two interconnected short metal arms are introduced between them. The relative angle between these arms can be modified by adjusting the screws that hold them together. This small modification allows the target to move

freely in the X-Y plane until it is at a desired relative position with respect to the substrate as shown in Figure 2.6. The rotational degree of freedom is attained with the help of the adjustable screw head.

Figure 2.4. Side view of target holder showing its connection to a turnable screw head

A provision is kept for another target to be attached to the target holder. This incorporation of an additional target can be achieved by using a screw assembly with the central arm of the target holder.The additional target can be used for two advantageous roles. Firstly, it can act as a beam block for incoming laser pulses that grazes the substrate. This prevents scattering of the laser beam from the walls of the chamber and reduces the chances of emitting

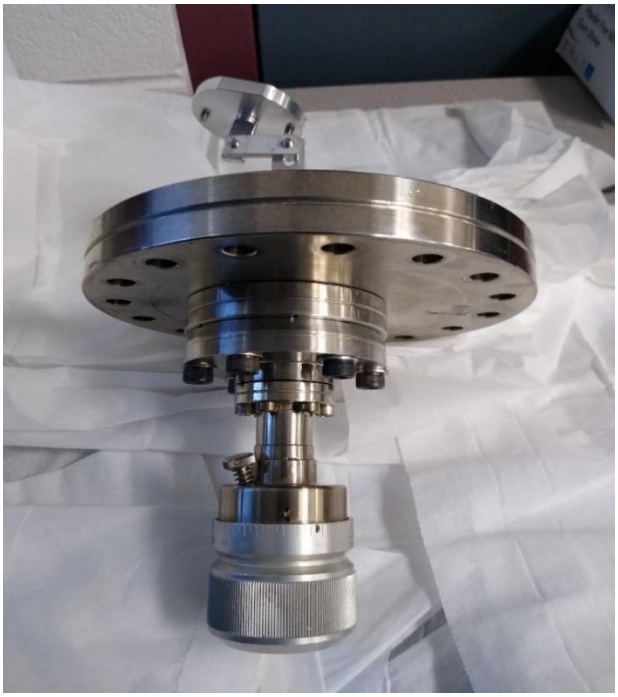

Figure 2.5. Front view of target holder with a magnified view of the target manipulator

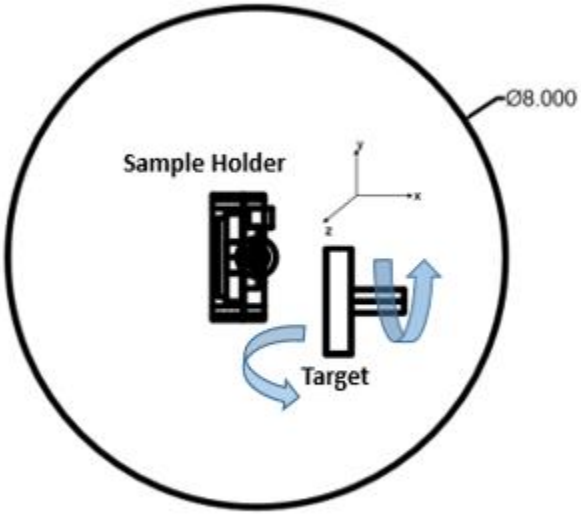

Figure 2.6. Schematic diagram showing side view of target holder with respect to sample holder

unwanted particulates (for example, the metal inside the chamber). Secondly, it can be used for mounting a target of a different material. In this latter arrangement, by controlling the laser pulses incident on the primary and secondary target respectively, we can deposit a doped semiconductor thin film. This can open a whole new dimension to thin film doping during deposition all happening simulataneously inside the same chamber.

2.1.4 Optical assembly. In order to perform PLD and CVD actions simultaneously in the same system, it is an essential requirement to have two separate beams. In order to achieve this, extensive testing is required for alignment optimization and establishing the right geometry. The primary idea behind the optical arrangement is to split the primary laser beam for CVD assisted PLD growth. One of the beams is used to ablate the target material, whereas the other beam serves to stimulate the reaction of the plume with the ambient process gas. To achieve this, a UV beam splitter is placed directly in front of the laser window as shown in Figure 2.7. This beam splitter causes 80% of the incident beam to be reflected off its frontal face while allowing

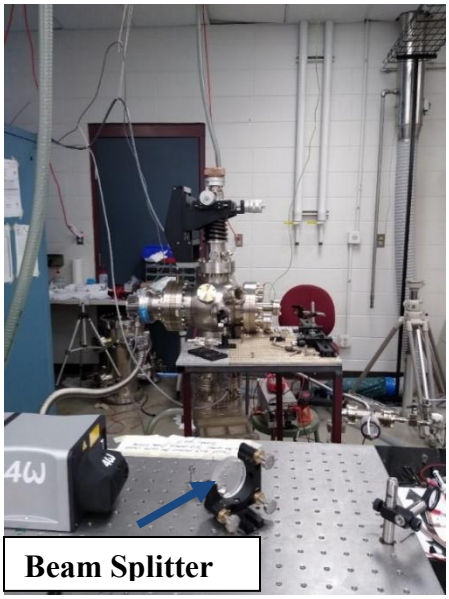

Figure 2.7. Side view of beam splitter

20% of the beam to be tranmitted through it. It is placed at an angle of 45^0 with respect to the normal to the laser beam exiting the laser source. The holder for the beam splitter is provided with adjustment knobs to change its relative angle in the X-Y plane. The reflected beam component from the beam splitter is designed to pass through a UV focusing lens fitted in front of the PLD laser beam window on the chamber. The focal length of the lens is chosen to be 12",which is the distance of the target from this focusing lens. This helps to create a focused beam having a shorter area of cross section for ablation and increases the energy density on the surface of the target during deposition. The transmitted beam component exiting the beam splitter is made to be incident upon a secondary UV mirror placed at 45^0 to the beam path before it can strike the tertiary mirror as shown in Figure 2.8 (a) and (b). In this arrangement, the edge of this secondary mirror is kept parallel to the beam splitter. This in effect rotates the

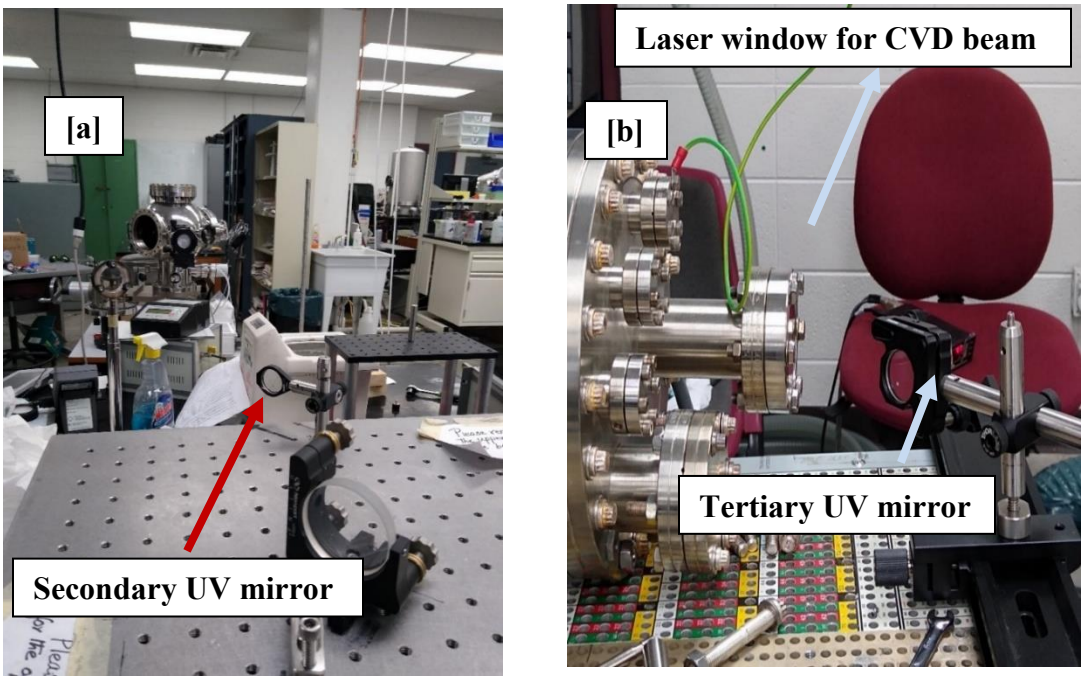

Figure 2.8. Position of (a) secondary UV mirror and (b) tertiary UV mirror

transmitted beam through 90^0. The combined effect of this set up leads to the creation of a secondary beam that is separate from the primary PLD beam. This secondary beam is finally incident on a tertiary UV mirror placed at 45^0 with respect to the beam. After suffering a 90^0 reflection off its surface, the beam finally enters the chamber through the secondary laser window. This beam is essentially used to pass above the substrate and stimulate CVD gas reaction. Thus, this leads to a primary beam causing the evaporation of target material and a secondar beam causing the reaction mechanism to occur close to the substrate before deposition as shown in Figure 2.9. It is important to note that only 20% of the intital laser energy is carried by the CVD beam due to the reasons illustrated above. This is desirable since more energy is

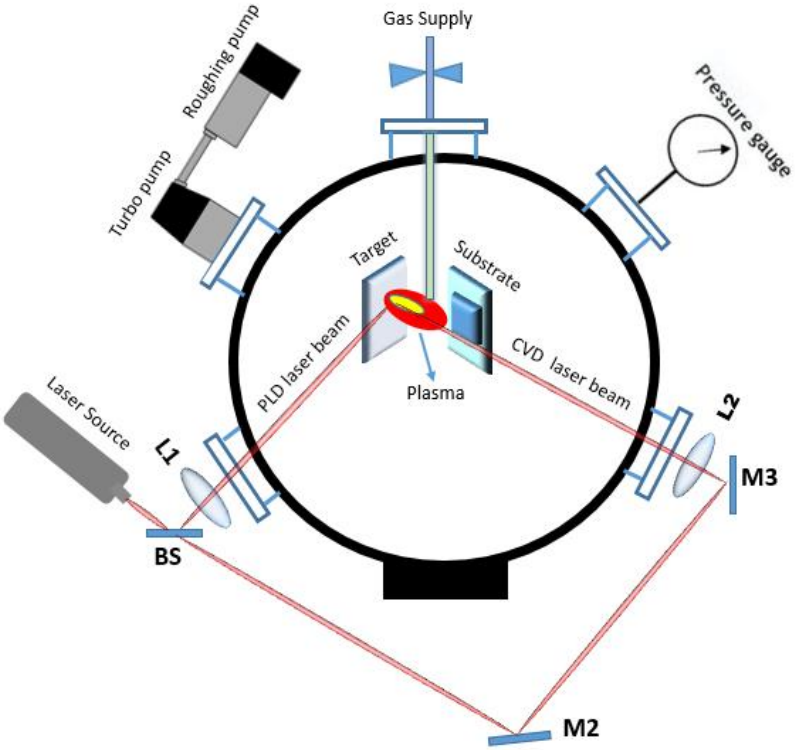

Figure 2.9 Schematic Layout of the CVD assisted PLD system

required in the primary beam as compared to its secondary counterpart, since its purpose is to "assist" the reaction. A focusing lens can be introduced between the secondary and tertiary mirrors. This imparts flexibilty in terms of choosing whether we want the secondary beam to be broad and defocused or narrow and concentrated depending on the application.

2.1.5 Gas handling. The gas handling assembly for the developed system is illustrated in the Figure 2.10 below. The system is custom built for handling up to three different types of process gases simultaneously. Overhead stainless tubes are used to guide the flow of process gases from the gas cabinet to the manifold valve. For safety purpose, each gas pipe if provided with ball valves before they connect to the manifold. The three pipes unite before entering and

Figure 2.10. Gas inlet and manifold valve

intermixing inside a single section before they are allowed to enter the chamber as illustrated in Figure 2.11. This short pipe section is connected to a leak valve and a Baratron gauge on its either side as shown in Figure 2.12. The leak valve allows the final introduction of process gas into the chamber. The gas pressure can be controlled by adjusting the opening of the leak valve. The mixing tube section is connected to a Baratron gauge which measures the pressure of the gas mixture. This arrangement further allows us to control the partial pressure of the individual gaseous elements in the mixture. It is important to note again over here that the Baratron gauge can only measure pressures up to 1000 torr. Thus, the total pressure of the gas mixture cannot

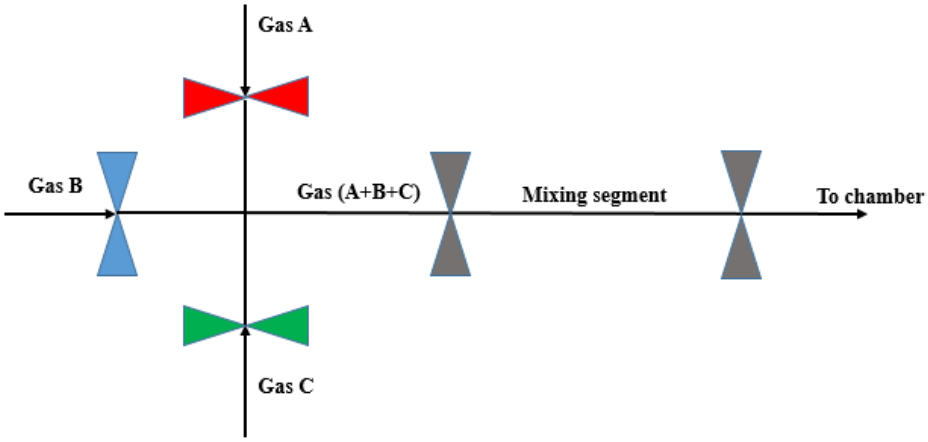

Figure 2.11. Schematic diagram of gas mixing system

exceed 1000 torr at any particular time for our applications. As process gas continues to be exhausted during deposition, additional gas can be reintroduced into the mixing tube as required. This allows for continuity of the process without compromising the safety of the sensitive instruments. A turbo-rotary pump assembly is connected on the downstream of the segment. A rotary valve opening is fitted before the opening to the turbo to allow selectivity in terms of

choosing pumping or purging action. During normal operation, even when the turbo pump is operational, the rotary valve is closed and the gas mixture enters the chamber through the leak valve. However, in case of accidental leakage, the rotary valve can be opened and the turbo vents all the gas contained inside the mixing tube. This arrangement allows for better preparedness against emergencies.

In order to prepare a gas mixture, we first begin with flushing the gas pipelines to get rid of any residual gas prior to deposition. Turbo pump is turned on and the rotary valve is opened. Each individual gas pipe is isolated by selecting the right combination of valves. Once a gas pipe has been isolated, all the valves on the pipe are opened right up to the gas bottle

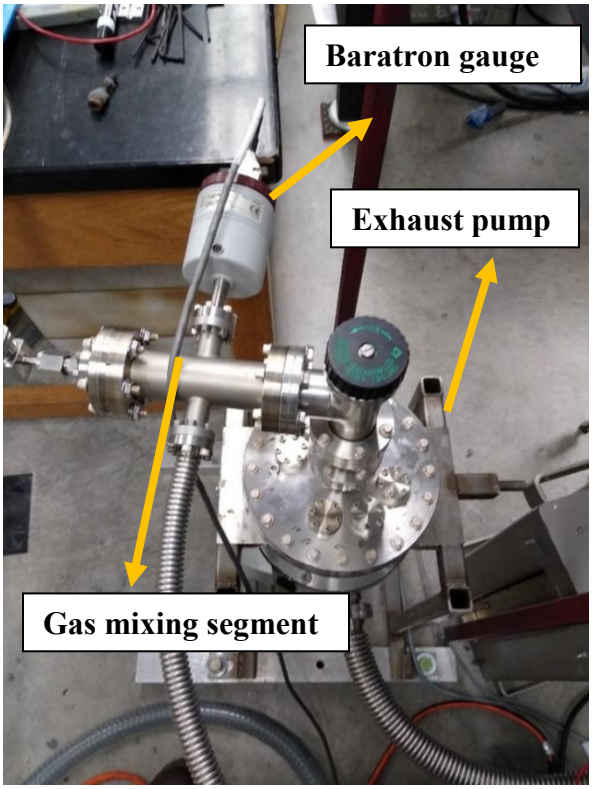

Figure 2.12. Magnified view of manifold valve and Baratron gauge

regulator until the pressure on the downstream regulator gauge reads at bottom of scale. This is process is repeated in a similar manner until all the pipes have been pumped down to vacuum. Now let us assume that the desired final mixture consists of gas A and gas B having partial pressures 400 torr and 40 torr respectively. We begin with gas A and introduce the gas into the pipeline by opening the valves all the way up to the mixing chamber. After doing the same for gas B, we have a gas flow line established all the way from the bottles to the mixing segment for both gases. Now we slowly introduce gas A into the segment and monitor the pressure on the Baratron gauge. Once the Baratron gauge reaches 400 torr, we stop the flow of gas A by closing the stop cock valve. Now, we follow the same procedure for gas B until the Baratron pressure reached 440 torr and shut off the valve for gas B. Thus, we are able to create a gaseous mixture having 400 torr of gas A and 40 torr of gas B. This technique can be used for preparing any gaseous mixture having different compositions than discussed in the example above as long as the total pressure does not exceed 100 torr.

2.1.6 Initial heater design. During the design of our system, we have explored two different types of heaters for heating the substrate inside the chamber. Each individual design along with its merits and demerits will be discussed in the following paragraphs.

Our first design consists of an UHV button heater (Model TB-170) manufactured by HeatWave Labs and rated for up to 1200^0C. This particular heater consists of a coil filament encapsulated in a metal body. Figure 2.13 shows the backside of the substrate holder with the heated embedded in it. The central cavity of the substrate holder accommodates a cylindrical metal piece made of molybdenum which in turn allows the frontal face of the button heater to make contact with it. This creates a continuous heat flow path from the button heater's face to the substrate when the latter is placed on the molybdenum piece. A special clip, slightly angled

at its tip, is used to secure the button heater and prevent it from falling off under the action of gravity when in its upright position. The lead wires of the heater are connected to copper wires through mini connectors. The copper wires are attached to a feedthrough with connection nodes to the exterior of the chamber. The exterior nodes when connected to an appropriate voltage source, complete the heater connection and current starts to flow through the coils. In our set up we use an AC variac to step down the line voltage to a 10V supply. Next, we

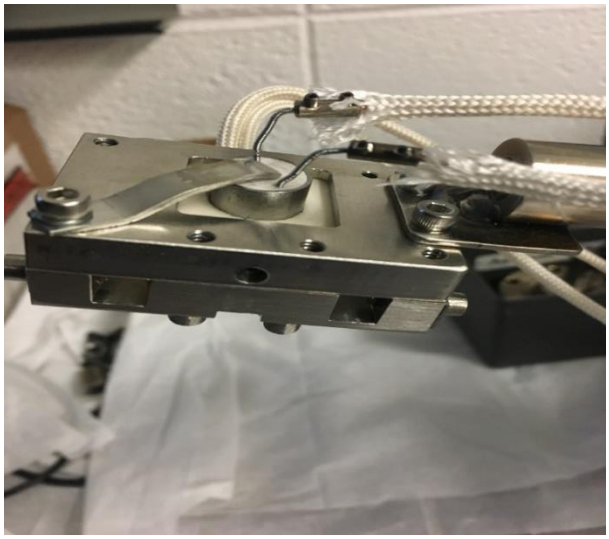

Figure 2.13. Rear view of UHV button heater attached to the substrate holder

connect another step down transformer to control the percentage output of the voltage obtained in the previous step and use it for the input supply voltage. This connection assembly helps to ensure that the maximum rated voltage of the heater is not exceeded under any circumstances and thus prevents any damage to the heater filaments. The copper wires are protected with UHV grade insulation material in order to prevent accidental short circuiting by touching other parts of the chamber. Furthermore, the lead wires of the heater and the copper wires were adjusted to

establish a secure connection while coping with the torsional stress in the wires when the central axis of the substrate holder is rotated to adjust the substrate position.

2.1.7 UHV heater calibration. The chamber was first pre-evacuated to a vacuum pressure of approximately 10^{-7} torr prior to testing. Figure 2.14 shows a glowing image of the heater during its calibration. For calibration purposes, we used a fine bare wire K-type thermocouple (Chromel-Alumel) and measure the voltage across its leads while the heater is operational and glowing. The thermocouple junction tip was sandwiched between the molybdenum piece on the substrate holder and the substrate itself. The same clips securing the

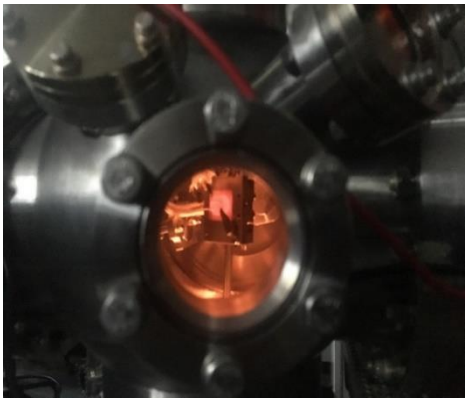

Figure 2.14. Snapshot of UHV button heater during operation

substrate in its position was used the hold the entire arrangement as described. The thermocouple lead wires were connected to a separate set of feedthroughs through fine insulated copper wires. The exterior connection ports to the feedthrough was connected to a voltmeter after identifying the positive and negative leads of the thermocouple. The voltage of the thermocouple leads are matched against the specification sheet to get the local temperature of the wire tips. In this way, we were able to measure the substrate temperature. As illustrated in Table 2.1 below, the temperature measurements plateaued around 300^{o}C which was below our expected value

according to the heater specifications. This implied improper functioning of either the thermocouple or the heater or even a combination of both. In order to test the possible sources of error, we carried out two more experiments. In the first scenario, two thermocouples of the same type (K) but having different diameters of 0.20" and 0.15" respectively were tested inside a tube furnace between a temperature range of 400-600 degrees. The tube furnace was sealed with

Table 2.1 UHV button heater calibration data with thermocouple

Thermocouple voltage (mV)	Heater current (A)	Supply voltage (V)	Chamber pressure (torr)
6.0	3.00	2.2	$6.8 * 10^{-6}$
7.0	3.02	2.2	$6.9 * 10^{-6}$
7.8	2.98	2.2	$7.7 * 10^{-6}$
8.0	3.00	2.2	$7.9 * 10^{-6}$
6.6	2.97	2.2	$8.0 * 10^{-6}$
6.2	2.93	2.2	$8.0 * 10^{-6}$
8.2	2.99	2.2	$8.0 * 10^{-6}$

plugs on either end with a steady supply of nitrogen gas inside the cavity. This was done to maintain an inert atmosphere inside the furnace and prevent oxidation of the bare thermocouple wires. As presented in the Table 2.2 below, the readings on the two thermocouples fairly agreed with each other as well as their theoretical values on the specification sheet. Next, we tested a different thermocouple having an inner diameter (0.003") placed between the substrate holder and the substrate which yielded higher temperatures than the former one having a 0.20" diameter

Table 2.2 Calibration data for thermocouple performance inside tube furnace

Furnace temperature (^{o}C)	0.20” thermocouple (mV)	0.15” thermocouple (mV)	Theoretical voltage (mV)
413	17.9	17.6	17.03
425	18.7	18.9	17.75
500	22.1	21.1	20.64
515	22.9	21.9	21.28
600	26.2	25.1	24.90
615	26.8	25.6	25.54
700	28.5	29.4	29.13
709	29.1	30.1	29.51

The outer walls of the chamber tested negative for short circuiting, ruling out another possible cause of loss in voltage indicating lower temperatures than actual. This helped us to eliminate the possible imperfections in the thermocouple wiring and implied that there were underlying issues within the chamber, particularly in the heater design.

2.1.8 Cold junction compensation In order to maintain accuracy of measurements during the calibration tests, we considered the effects of cold junction compensation of the thermocouple wire leads and factored that into our calculations. Since the lead terminals of the thermocouple as placed in our system are at room temperature instead of 0^0 C, this could lead to erroneous temperature readings if not considered. For this purpose, a separate experiment is set

up where the thermocouple junctions are placed in an ice bath and the voltage across the leads are measured. This voltage is recorded (-1 mV) and is subtracted from every other voltage reading obtained during the real time operation of the heater. This adjustment finally helps to makes sure that the thermocouple integrated in our system is cold junction compensated.

2.1.9 Performance evaluation of UHV heater. Although the specification sheet of the UHV heater displays a maximum temperature of 1200^0 C when operating under maximum power, the maximum temperature recorded during the calibration test was approximately 400^0 C. The same test when carried out with the thermocouple junction attached to the front face of the heater directly without any substrate or holder yielded a temperature of 700^0 C. This problem can be primarily attributed to the large thermal mass of the substrate holder. The other possible cause of error could be a weak contact between the molybdenum metal piece holding the substrate and the front face of the heater. This is possible due to the expansion of both metal bodies due to the heat generated during operation. Hence, in order to build a system capable of reaching up to at least 800^0 C, we had to reconsider and redesign our heating system.

2.1.10 Modified heater design. The design of the modified heater is shown in Figure 2.15 below. A piece of silicon wafer forms the integral part of this design. The wafer rests on two copper clips placed on either edge of the removable piece of the substrate holder. A pair of clips is used to hold both the substrate and the silicon piece firmly in its position. A different set of metal clips, placed on the bottom piece of the substrate holder, makes contact with the copper when the removable piece is attached to it. The clips are attached to insulated copper wires that are connected to the same feedthrough discussed in the design of the UHV button heater discussed in the sections above. To prevent short circuiting of the metal parts, a special set of ceramic screws and washers are used to connect the copper lead wires to the substrate holder

as shown in Figure 2.16. The connecting clips are raised at height above the frame of the substrate holder to prevent contact with the stainless steel base. Also, the clip is designed to accommodate a certain degree of flexibility to allow a spring action whenever the removable

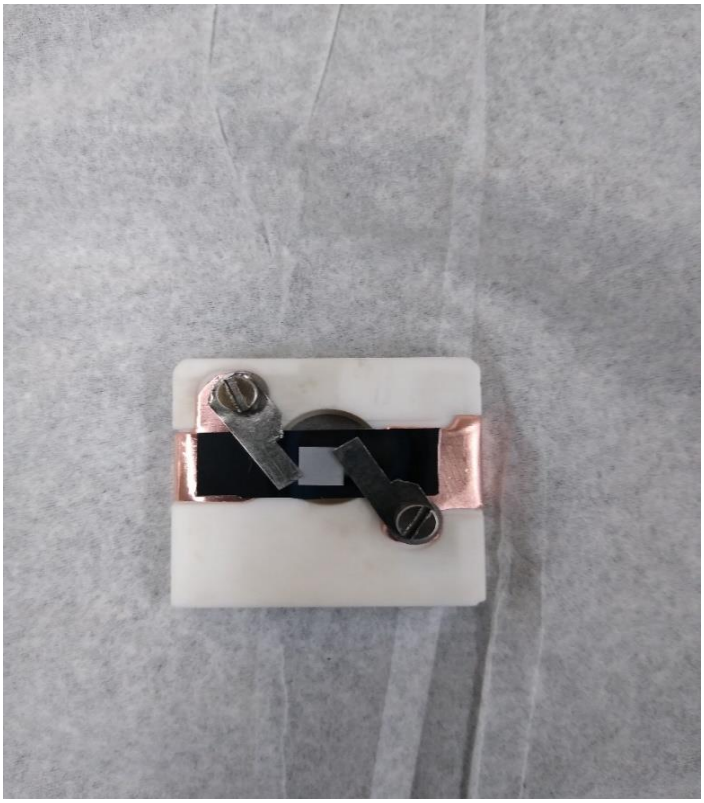

Figure 2.15. Design of modified heater using silicon wafer and copper clips

substrate holder stage is inserted to load a new sample or removed post deposition. This makes the system user friendly and reusable. However, the only consideration is that, for each new sample load, the silicon wafer needs to be replaced as it is coated with deposited film material.

The semiconductor properties of silicon is well utilized in this design. The resistivity of silicon decreases with increasing temperature, allowing more current to pass through it at higher temperatures. Thus, once a current flow has been established through the wafer, it becomes a

spontaneous process which makes it possible to reach temperatures as high as 1200^0 C (still below the M.P of Silicon, i.e., 1400^0 C) at a much faster pace as compared to the previous design. A special grade of silicon wafer having low resistivity is selected. Further, the wafer is subjected to wet chemical etching using hydrofluoric acid to get rid of the silicon dioxide layer on top of it. This is critical step since the oxide layer which forms naturally due to atmospheric

Figure 2.16. Lead wire connections of the modified silicon heater

oxidation is insulating in nature and may inhibit the passage of current if not etched off. Finally, a D.C. constant current source supply is connected to the feedthrough port on the exterior of the chamber which completes the circuit and triggers the initial current flow in the system.

2.1.11 Calibration of modified heating element. An infrared thermometer is used to calibrate the heating system discussed in the above paragraph. First, the emissivity factor setting

of the instrument is tuned to match that of silicon. Next, the viewing lens is focused directly on the wafer while current is flowing through it. The temperature of the wafer can then be read directly from the instrument display screen.

It is observed that, the silicon wafer starts to glow at a temperature of approximately 550^0 C and at a current value of 5.8 A as shown in Figure 2.17. However, due to the gradual decrease

Figure 2.17. Snapshot of modified silicon heater glowing during operation

in resistivity, the net power decreases. This problem is overcome by fine tuning the supply current until the infrared thermometer shows a stable temperature reading. For our uses, we were able to reach temperatures up to 800^0 C which was our highest targeted growth temperature. However, as mentioned earlier, the system is capable of reaching higher temperatures if necessary. Thus, this improved and ergonomic design allowed us to overcome the problems due to the limited scope of our previous design.

2.2 Characterization Techniques

For characterizing the films post deposition we have employed a variety of characterization tools. The following submenus contain a brief description and working principle of each technique.

2.2.1 X-Ray diffraction. X-Ray Diffraction is a characterization tool used for the structural analysis of crystalline compounds. Figure 2.18 schematically illustrates the geometric arrangement of an X-Ray Diffractometer. An X-Ray having a specific wavelength is used to bombard the target material when it undergoes scattering due to the atoms inside the crystal. The intensity and the pattern of the scattered beam picked up by the detector depends on the planar arrangement inside the crystal and can be used to extract meaningful information like the crystal phases present in the material. This diffraction process is based on Bragg's Law:

$$2d \sin \Theta = n\lambda \qquad (4)$$

Where d= inter-planar spacing, Θ= angle of incidence, n =order of diffraction and λ=wavelength.

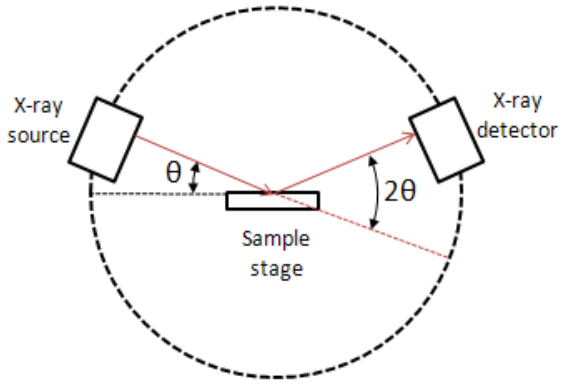

Figure 2.18. Schematic diagram of X-Ray Diffractometer [30]

We use a Bruker Discover D8 X-Ray Diffractometer having a Cu K□□X-ray source with a wavelength of 1.5406 angstroms. For typical Θ-2 Θ scans, the position of the detector is varied between 20^0 and 80^0. During the scans, we use a step size of 0.02^0 with a scan speed of 2.5seconds/step.

2.2.2 Scanning electron microscopy (SEM). SEM works on a similar principle as optical microscopes except for the fact that it uses electrons for imaging instead of visible light. An electron gun is used as a source of electron beam that is focused on the sample using magnetic lenses. This electron beam is rastered or moved horizontally across the sample surface and the information of the reflected signal is processed by the detector to create an image. Figure 2.19 shows an overview of the above process. Depending on the level of interactions with the surface, there can be three types of reflected particles, i.e. back scattered electrons, secondary electrons and X-Rays as shown in Figure 2.20. Back scattered electrons (BSE) are simply

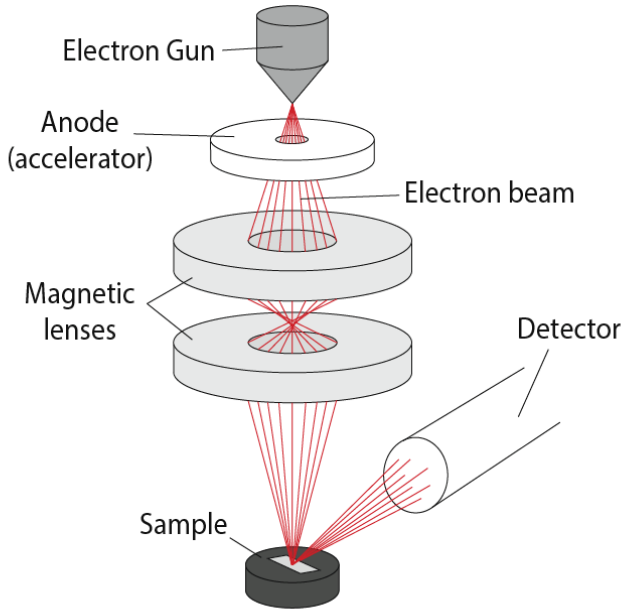

Figure 2.19. Schematic of Scanning Electron Microscope [31]

reflected off the surface while secondary electrons (SE) are generated due to the inelastic nature of interactions between the sample and the incident electrons. These two kinds of electrons are used for imaging purposes in SEM. The third kind of signal are X-Rays generated from deep within the sample. Since every element has its own characteristic X-ray, this can be used for elemental analysis of the sample and studying its composition. This X-Ray detection technique is utilized in Energy Dispersive X-Ray Spectroscopy (EDS).

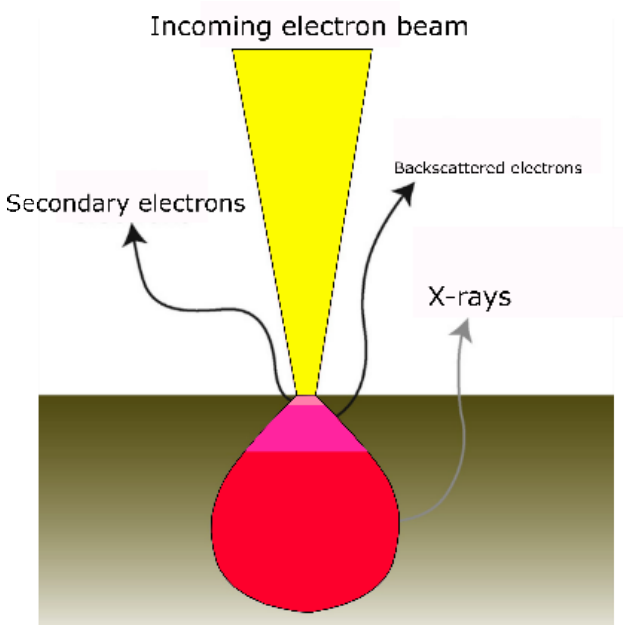

Figure 2.20. Different types of signals used in SEM and their area of origin [32]

The SEM and EDS analysis of our samples were performed using the Fei Quanta 250 instrument. However, the EDS of the latest samples were carried out using AZtecAM Ultim Max 170.

2.2.3 Raman spectroscopy. This is a non-destructive analysis technique that utilizes light scattering for the identification of crystal structures, chemical bonds and phases in a

material. When the sample is illuminated with a high power laser source, most of the reflected photons have the same wavelength as that of the incident beam and is called Rayleigh scatter. However, a small portion of the scattered photons have a different wavelength than the laser source and is called the Raman scatter as can be seen from Figure 2.21. The pattern of the scattered beam depends on the chemical structure of the sample and conveys meaningful information like chain vibrations and lattice modes.

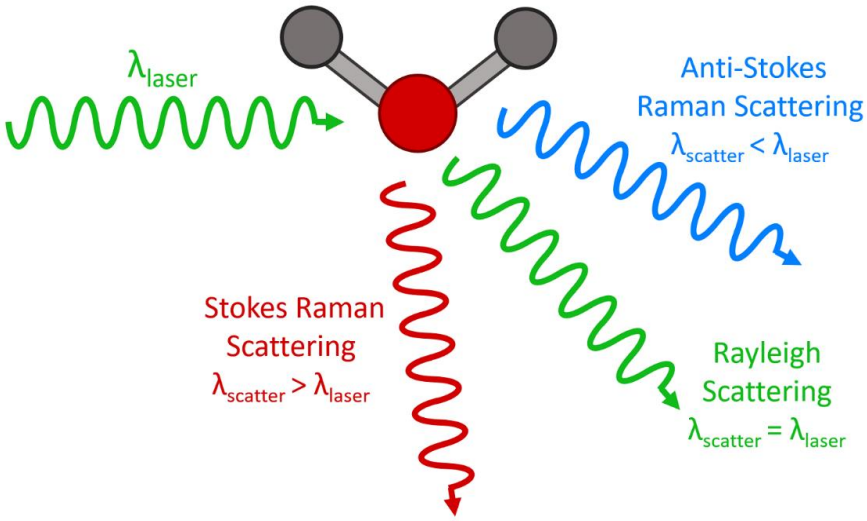

Figure 2.21. Principle of Raman Spectroscopy [33]

For our experiments, we have used a Horiba Labram HR Raman PL System. The laser source used was a UV green laser having a wavelength of 532nm and all spectra were recorded at room temperature. All data were collected over an acquisition range of 200 cm^{-1} to 1800 cm^{-1}. The acquisition time was set at 30 seconds and the time average of 10 such cycles were used for each spectrum of the samples under investigation.

2.2.4 Atomic force microscopy (AFM). AFM is a versatile tool frequently used for studying surface topography as well as mechanical, electrical and functional properties of

nanoscale materials. In this technique, a micro-tip probe attached to a cantilever is used to survey the sample surface. As the tip approaches the surface, it comes under the influence of attractive and repulsive forces and the cantilever is deflected accordingly. A laser and photodiode assembly is used for detection as shown in Figure 2.22. Corresponding to the movement of the cantilever, the reflected laser beam changes direction and the corresponding signal is picked up by the photodiode. This process is used to generate a special profile of the sample under investigation.

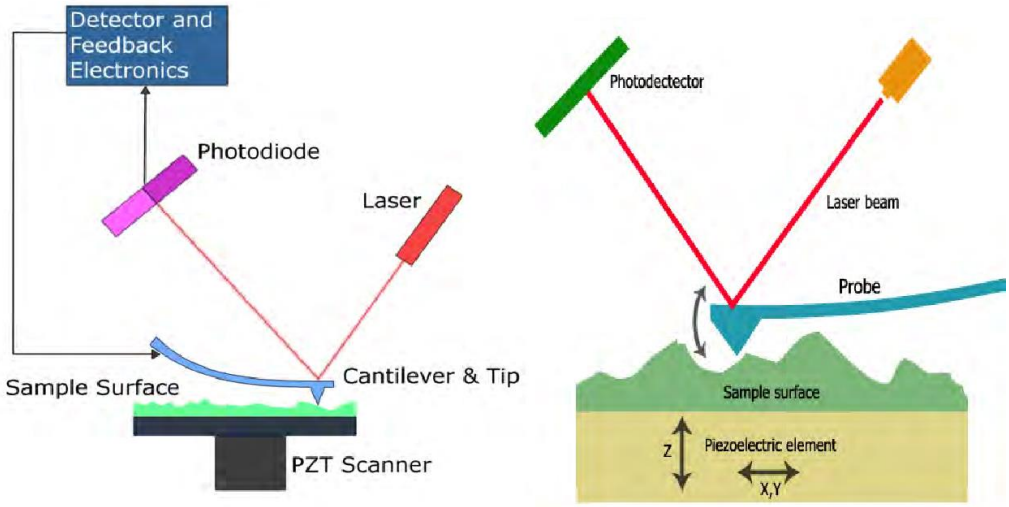

Figure 2.22. Working principle of AFM [34]

The AFM analysis for our samples were conducted at Jordan Valley Innovation Centre, Springfield, Missouri.

2.2.5 Profilometry. Profilometers are used for measuring features like surface roughness, film thickness and surface variations of samples. The basic operating principle of a profilometer is illustrated in Figure 2.23. It usually consists of a diamond tip called the 'stylus' that is used to establish contact with the sample surface. The stylus is moved laterally across the surface for a

specific scan length and its displacement as a function of its position is used to construct a vertical profile of the sample along the scanning length.

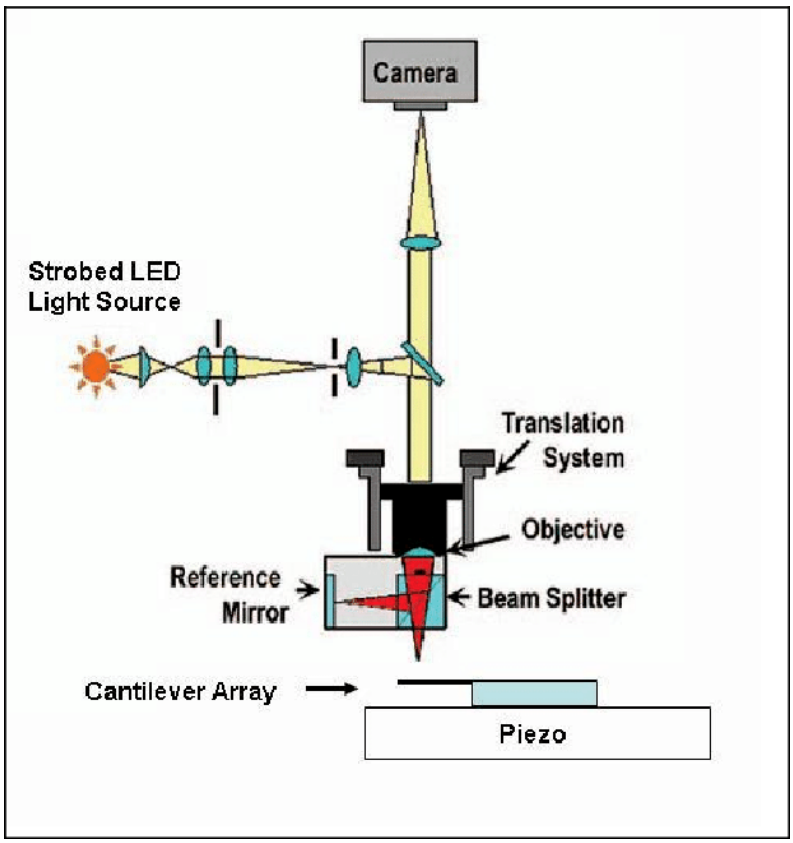

Figure 2.23. Schematic diagram of Optical Profilometer [35]

In order to measure the thickness of our films we have used Veeco Dektak 150 surface profilometer. The instrument has a vertical resolution of 1 angstrom over a range of up to 1mm. The available options for the stylus radius are between 50nm to 25 microns. For our measurements, a stylus of radius 12.5 microns was used with a force of 3.00 mg. All scans were performed at a speed of 5 microns/second over a scan length of 300 microns.

2.3 Initial Design Testing

In order to test the design of our system, we first performed a Pulsed Laser Deposition of Nickel metal on a silicon (1 1 1) wafer substrate. For this particular experiment, the growth was carried out at room temperature and in the absence of any background gas. The laser was operated at a frequency of 10 pulses per second having a Q-switch delay of 10 micro seconds for a total of 500 shots. The base pressure of the chamber during operation was maintained at 10^{-8} torr.

The grown film was first inspected using Scanning Electron Microscopy as shown in Figure 2.24. The spot size and the voltage were fixed at 3.5 and 5kV respectively. At a magnification of 1041x, micro granules of deposited material on the silicon were visible. At

Figure 2.24. SEM image of Nickel film on Silicon grown at room temperature

higher magnifications of 7128x, we observe droplets which upon EDS analysis prove to be composed of Nickel. However, in addition to the droplets, we observe smoother regions in its periphery whose image cannot be resolved to get additional features upon further magnification.

In order to examine the composition of the finer regions, an EDS scan was carried out as shown in Figure 2.25 (a) and (b). Once again, the EDS scan displayed Nickel peaks. In addition to the Nickel, we also observe peaks of Silicon originating from the substrate and Carbon due to organic contamination of the SEM chamber.

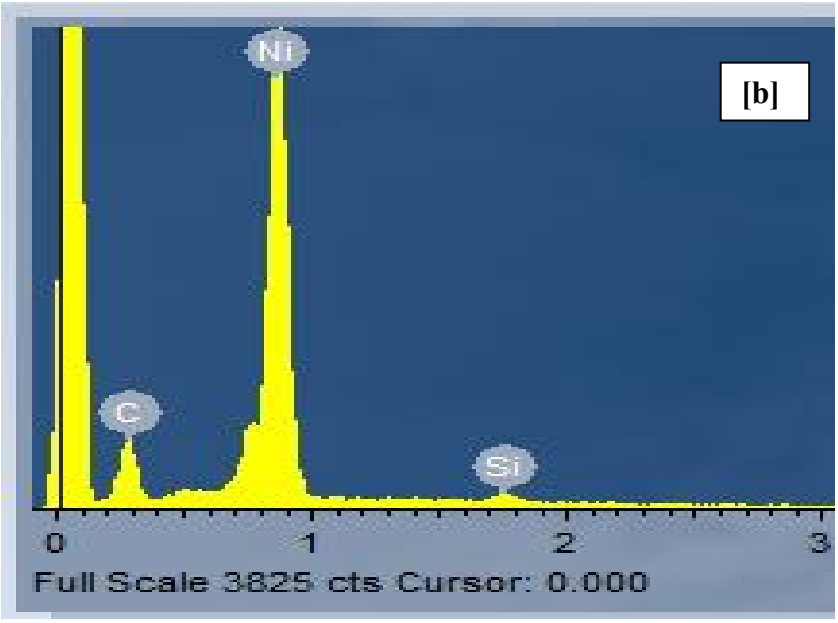

Figure 2.25. (a) SEM image showing smooth regions of Ni film in the periphery of the droplets and (b) EDS spectra of the smoother film regions confirming the presence of Nickel

Next, we perform X-Ray Diffraction analysis of the film using theta-2theta scan using a Cu K-alpha X-ray source having a wavelength of 1.54 A^0. In the XRD scan shown in Figure 2.26, we observe only peaks from the Silicon substrate and no Nickel peaks were visible.

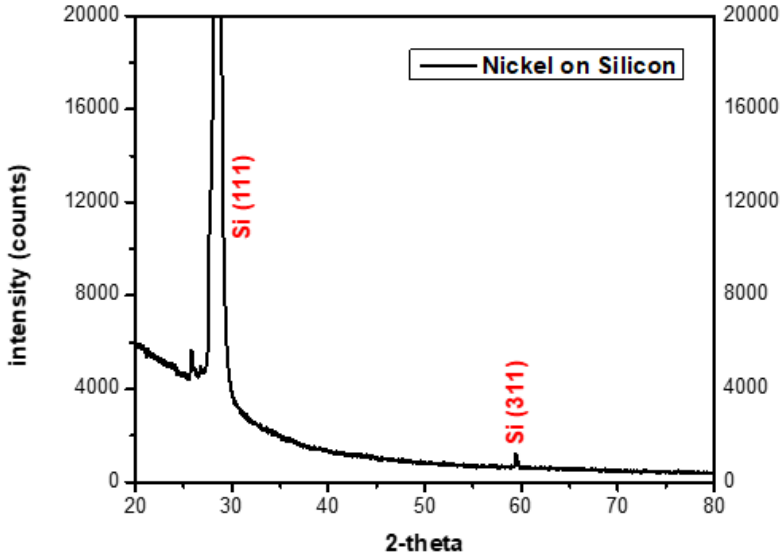

Figure 2.26. XRD data of Nickel film on Silicon at room temperature

From the EDS scans, we conclude that the deposited film is mostly smooth in addition to a few droplets. Although the XRD fails to reveal any crystallinity, this can be attributed to lack of substrate temperature resulting in amorphous growth. However, it proves that film deposition can be carried out in the chamber which meets our initial goal. This gives us the leverage to advance our experiment and testing the growth under gaseous environment.

2.3.1 Incorporating CVD with PLD. For this phase of the experiment, we attempt growing a Nickel Nitride (Ni_3N) film as a case study. This was accomplished by incorporating a CVD beam of Nitrogen gas in addition to the existing PLD set up. Figure 2.27 offers a closer

view of the exact geometry between the CVD and PLD beams relative to each other. The growth was carried out at room temperature on the same Silicon substrate as described earlier. At first, the chamber was evacuated to a base pressure of 10^{-8} torr.

Next, the chamber was cleansed using Nitrogen gas in order to get rid of any residual impurities prior to the deposition. The chamber pressure was held stable at $5.8*10^{-6}$ torr during the deposition. The laser parameters were kept the same as in the earlier experiment. However, the number of shots was increased to 5000.

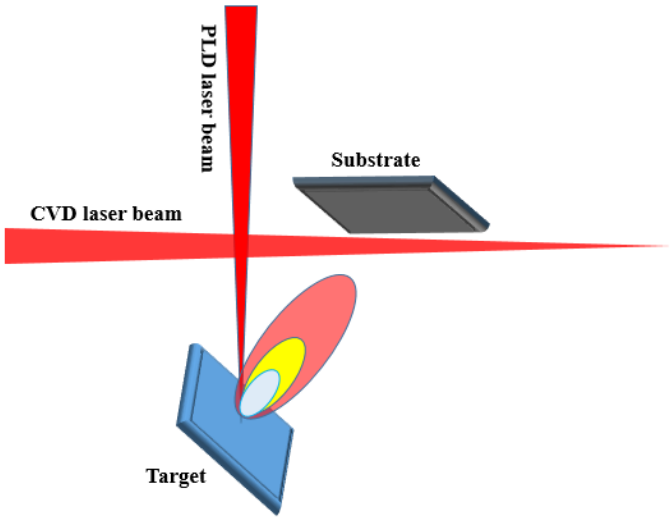

Figure 2.27. Magnified view of the geometry between CVD and PLD beam

We characterized the grown film using SEM, EDS and XRD analysis. The XRD still failed to show any conclusive signs of crystallinity. It is important to mention here that we encountered a serious problem which made the EDS analysis a challenge for this and future experiments whenever we attempt to grow a Nitride film on a substrate which is either an Oxide

or prone to get oxidized over time. The Nitrogen signal on the EDS spectra shown in Figure 2.28 is below the detectable limit and shows a poor signal to noise ratio. The Oxygen signal from

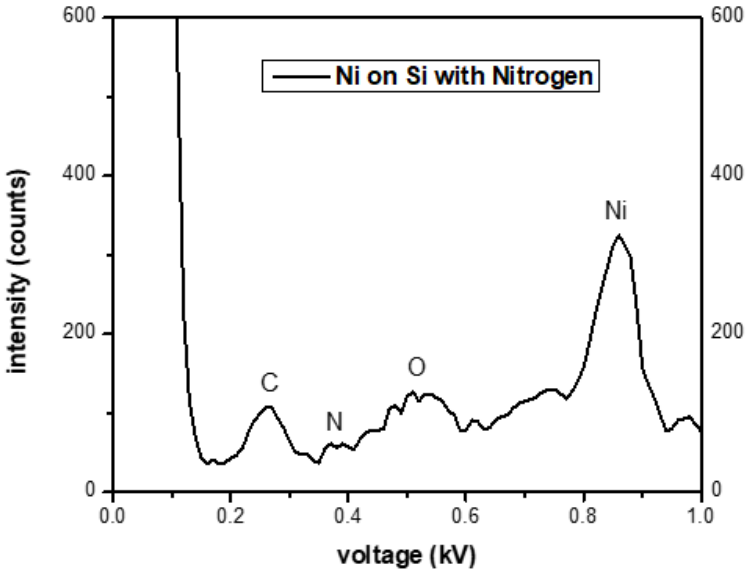

Figure 2.28. EDS spectra of Ni film deposited with nitrogen gas CVD on Silicon substrate

the silicon substrate (due to natural aerial oxidation and formation of Silicon Dioxide layer on top) situated at 0.525 keV has a high count and makes it even more difficult to resolve the Nitrogen line at 0.392 keV which falls right next to it. The Carbon line observed at 0.27 is from organic contamination due to manual handling of the film. Hence, although we observe a small Nitrogen peak, a conclusive evidence cannot be drawn regarding the formation of a Nitride film.

These results lead us to investigate the apparent future and consider feasibility of the reaction under the conditions described above. After careful consideration, we were able to identify a number of factors that could be restricting the growth of our desired film. The lack of high temperature in the substrate continues to be a possibility for not producing a crystalline film

as mentioned in the previous section. In addition to that, the high bond energy for the Nitrogen triple bond (945 kJ/mole) is another issue which makes the dissociation of the process gas a challenge especially with the 266nm laser used in our experiment. Without sufficient bond dissociation, there is an inadequate supply of free Nitrogen atoms available for reaction with the Nickel atoms in the PLD plume hindering the film growth. Lastly, the role of the geometry of the substrate could also play a significant role. Silicon, although widely used as a substrate for growing a wide array of films has a cubic structure as opposed to the hexagonal structure in most Nitrides. Thus, we try to consider the effect of changing each of these parameters in our subsequent experiments.

2.3.2 Change of process gas. Following our hypothesis in the previous section, we designed this new experiment to study the effect of the role of altering the process gas and its effect on the reaction dynamics. For this purpose, we introduced a different Nitrogen carrying gas, i.e., Ammonia (NH_3) as the process gas. All other experimental parameters were preserved from the previous step. This controlled change in the experimental design would allow us to isolate and focus on individual experimental parameters (in this case the process gas) and enable us to optimize the system. The H-NH_2 single bond in NH_3 has a bond energy of 435 kJ/mol which is significantly lower than the N-N triple bond in Nitrogen when compared. Thus, it would have a higher probability of dissociation and favor the reaction mechanism. Furthermore, to get a better view of the Nitrogen signal on the EDS spectra, the silicon substrate was wet chemically etched with hydrofluoric acid (HF) to remove any silicon oxide layer present on its surface. The XRD and EDS results are shown in the Figure 2.29 (a) and (b) below. With no characteristic peaks of Nickel Nitride in the diffraction pattern, commenting on the crystallinity of the film still remains a difficult task. In order to get the strongest Nitrogen signal, the acquisition time was

increased to 600s from the default 180s. This was done with the idea that the extensive acquisition would average out the noise and yield a better count for the Nitrogen signal. This would also increase all other real signal including contaminants. The scan voltage was kept relatively low at 2kV in order to avoid deeper penetration of the electrons into the substrate and get more X-rays from the film instead. Also, different regions of the film were surveyed and the scan size area was varied. However, although hints of Nitrogen was observed on the EDS spectra, still its presence could not be confirmed with certainty.

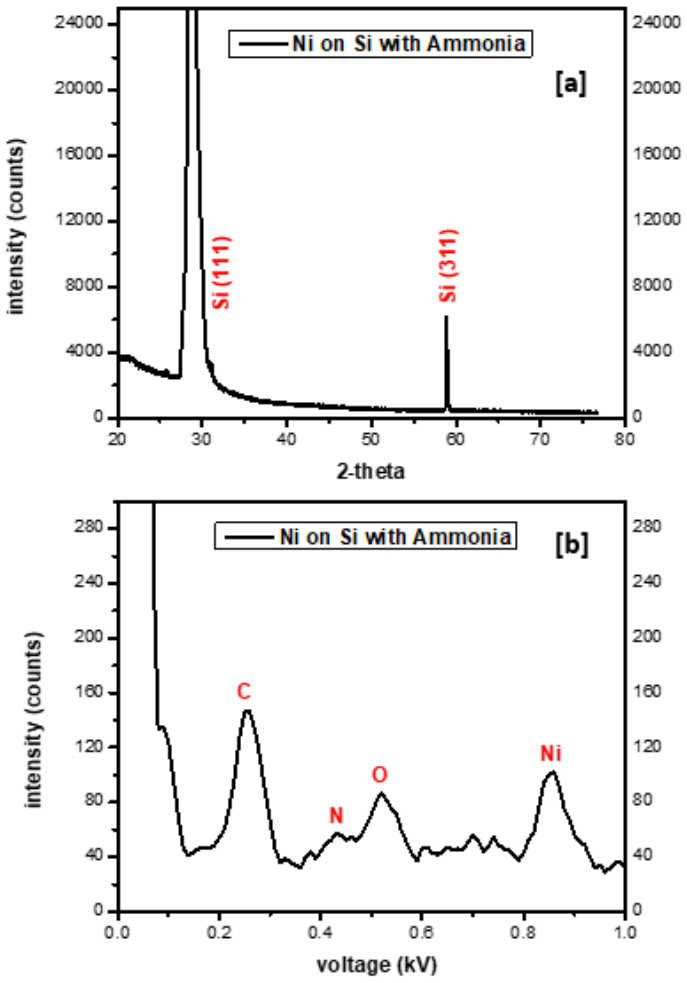

Figure 2.29. (a) XRD data for Nickel on Silicon with Ammonia gas CVD and (b) EDS data for Nickel on Silicon with Ammonia gas CVD

2.3.3 Growing at elevated temperature. From our previous experiments we were convinced that, temperature, a factor that we did not include until this point could play a vital part in the reaction. Besides, as discussed in the previous segments, the choice of substrate and its implications on the film growth still needed to be explored at this stage. After taking these into consideration, we modified our experiment to be performed at elevated temperature and using a different substrate. While fixing all the other parameters in the previous step, we raised the growth temperature to 386^0 C by incorporating the UHV button heater and used sapphire (Al_2O_3) as our substrate. This was done with the expectation that the geometry of the sapphire substrate would provide better conditions for the film growth. Further, the substrate was annealed prior to the film growth in order to relieve any stress in its morphology and flatten out the grains if any. Additionally, an external change was also made in the system. We redesigned the optics to include a DC optical chopper in tandem with the PLD beam. The frequency of the chopper was adjusted in a way so as to chop the PLD beam in a 1:4 ratio with respect to the CVD beam. This implies that the CVD beam would have four times as many pulses as compared to the PLD beam during the total span of 5000 laser pulses. The increased duration of the CVD beam was expected to give the plume ample time to interact with the ammonia gas before the arrival of the next batch of particles freshly ablated from the target. Additionally, we also explored different methods of focusing the CVD beam. In some cases, the CVD beam was narrowed down using a focusing lens and allowed to graze the substrate, while in other instances, it was allowed to be broad and defocused during its incidence on the substrate. The narrow and focused beam could maximize the reaction probability by concentrating a greater number of photons close to the substrate and meeting the energy barrier. On the other hand, the broadened

beam could enhance the interaction of the plume with the process gas due to the increased reaction cross sectional area.

The XRD and EDS plots from this experiment are shown in Figure 2.30 (a) and (b) respectively. Aside from the dominant sapphire peaks originating from the substrate, we did not

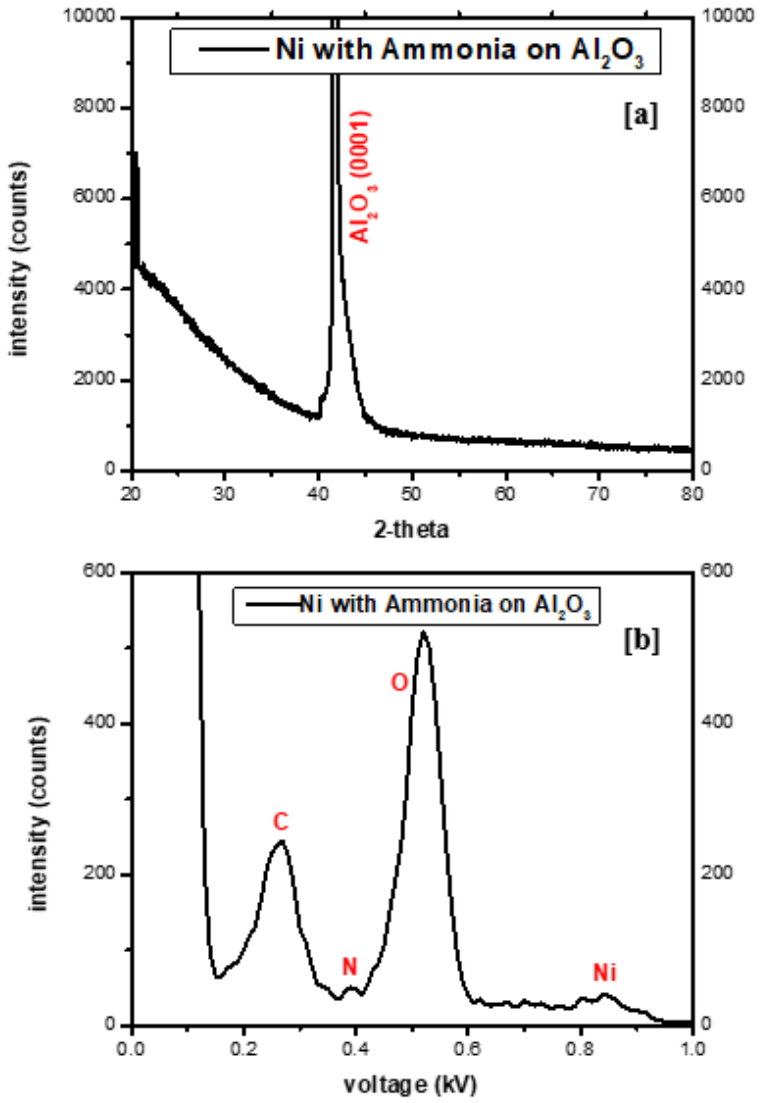

Figure 2.30. (a) XRD data of Nickel film on Sapphire with Ammonia gas CVD at 386^0C and (b) EDS data of Nickel film on Sapphire with Ammonia gas CVD at 386^0C

observe any characteristic peaks for Nickel Nitride on the XRD. The EDS plot did not demonstrate any pronounced observe any characteristic peaks for Nickel Nitride on the XRD. The EDS plot did not difference in its spectra and the Nitrogen signal was still fairly weak to draw any conclusions. At this point it was evident that there is a requirement to find an alternative solution for triggering the reaction. One possibility could be exploring the growth of a different metal nitride film by changing the metal target. As different metals have different enthalpies of formation during the nitration process, it would not be surprising if the existing reaction conditions preferred the growth of one particular nitride over the other. On the other hand, the precursor gas could be reimagined in ways that would catalyse the overall process. We discuss these modifications and their results on the system performance in the next segment.

2.3.4 Target dependencies. At this stage of our experiment, we inspect the effect of changing the metallic target on the reaction feasibility. We chose Aluminum metal as our new target for two specific reasons. Firstly, the hexagonal crystal structure of aluminum nitride is expected to show better film alignment when grown on sapphire substrate owing to the symmetry between them. Secondly, from an energetics point of view, the nitride formation is more favorable with Aluminum when compared against that of Nickel. This is corroborated by the fact that the standard enthalpy of formation of Aluminum Nitride (AlN) is -317.98 kJ/mol which suggests that the reaction is spontaneous in nature. This means that that once the reaction is initiated, it should drive itself to completion without any significant external energy input.

2.3.5 Nitriding potential. The change in target was also accompanied with a slight modification in the process gas in order to catalyze the nitride formation. Instead of using a single supply of ammonia gas, we infuse a calculated amount of hydrogen gas to create a gas mixture. This is a popular technique used in gas nitriding applications and has potential

advantages. The key here is to adjust a crucial parameter called the "Nitriding Potential" which measures the ratio partial pressures of ammonia gas relative to hydrogen. [36] The dissociation reaction of ammonia gas is shown below:

$$NH_3 \longrightarrow [N] + 3/2\ H_2 \qquad (5)$$

Since the above reaction is reversible in nature, the relative concentrations of ammonia and hydrogen mostly dictate the direction in which the reaction proceeds. If there is a high concentration of hydrogen, the dissociated nitrogen atoms may recombine with it to form ammonia and hence slow down the reaction. Thus, for monitoring the reaction rate such that nitrogen formation is enhanced, the nitriding potential was thermodynamically defined and formulated as:

$$K_n = P_{NH3} / P_{H2} \qquad (6)$$

where K_n is the nitriding potential coefficient and P_{NH3} and P_{H2} are the partial pressures of ammonia gas and hydrogen respectively. This further implies that the lower the partial pressure of hydrogen, the greater is the nitriding potential. In order to use this strategy effectively, we filled up the gas manifold (described in the engineering section) with ammonia and hydrogen such that hydrogen only constituted 10% of the mixture, in terms of partial pressure. The manifold pressure as measured by the baratron gauge was 520 torr prior to the deposition. The deposition temperature was 386^{o}C and the chamber pressure after a steady gas flow was established was recorded at 6×10^{-3} torr. Since the primary goal of this experiment was to examine whether the nitriding process aids the film growth, the optical chopper was excluded for this particular run. Instead, the number of laser shots was increased to 24,000 with the same laser parameters as before. The CVD beam was defocused and directly incident on the substrate. However, upon characterization using XRD and EDS, our newly grown film did not reveal any

distinguishable new features. As mentioned before, this gave rise to an ambiguity in terms of resolving whether there is an issue in the process parameters resulting in film growth or the sensitivity of our EDS spectrometer. In order to tackle these existing complexities, we had to consider an alternative characterization route that could yield explicit results. Interestingly, aluminum nitride being a Raman active element, has clear peaks that are separate from the sapphire substrate. Furthermore, due to the presence of different phonon vibration modes in the compound, there are multiple Raman peaks corresponding to the individual modes. Due to the combined effect of the aforementioned reasons, Raman spectroscopy seemed to be a promising approach for characterization. Although preliminary Raman analysis did not reveal any notable characteristics, the film showed hints of Aluminum Nitride Raman signatures upon annealing at 800^0C in Nitrogen atmosphere for 10 hours. Thus, it encouraged us to recalculate the process parameters so as to include further increase in temperature as well as exposure to Nitrogenous carrier gas.

2.3.6 Optimized conditions specific to aluminum nitride growth. To proceed with our hypothesis, we deposited our latest films using the CVD assisted PLD method on Si (100) and Al_2O_3 (0001) substrates. Our aim was to compare and study the film growth at two different values of temperature that is above the range of our previously grown films. Hence, the depositions were carried out at two different temperatures, i.e. 600^0C and 800^0C for each substrate. During the deposition, the PLD beam was chopped at regular intervals while the CVD beam was kept running until the end of the experiment. The deposition process followed a cyclic order of 2,000 shots of PLD+CVD action followed by 1,000 shots of CVD for a total of 8 such cycles. Thus, the total number of laser shots used was 24,000 although only 16,000 of them were dedicated PLD shots. The composition of the process gas mixture and the laser parameters were

kept fixed as in the previous experiment. The ambient gas pressure was maintained at 10^{-5} torr and 10^{-4} torr respectively for the PLD+CVD and CVD cycles. The films were annealed post deposition in the same Ammonia-Hydrogen environment for one hour at the same growth temperatures.

PERFORMANCE RESULTS

3.1 X-Ray Diffraction

Figures 3.1 (a) and (b) show the XRD patterns obtained for the Aluminide Nitride films grown on Silicon (100) substrate at deposition temperatures of 600^0C and 800^0C respectively. Initial observation only reveals the dominant Si (400) peak at 69^0 originating from the substrate. However, upon careful investigation (shown in the magnified view), we observe the AlN (100) crystalline peak at 33.06^0. The absence of any other characteristic peaks of AlN confirm that the as-grown films were single phase. The squashing of Si (100) and Si (200) peaks can be due to XRD extinction rules resulting in the visibility of only (400) plane in Silicon. [37] The rocking

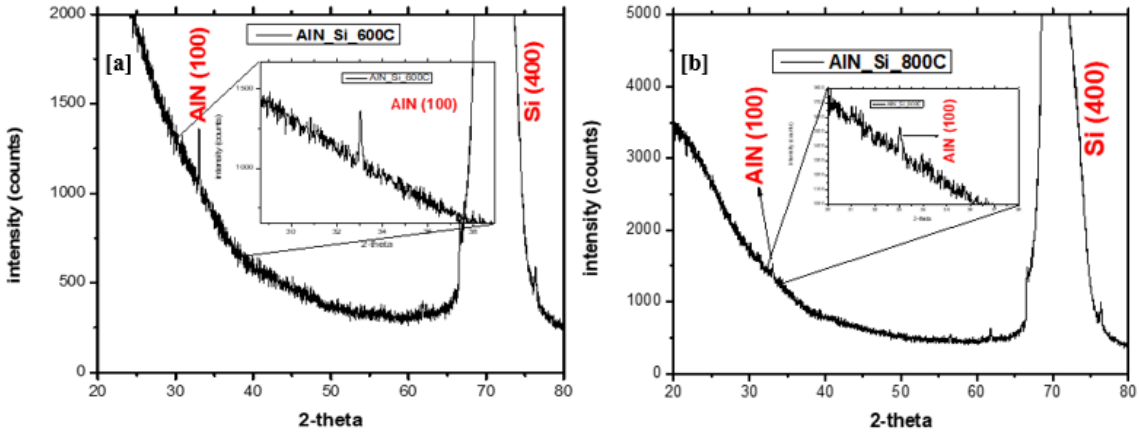

Figure 3.1. XRD results for Aluminum Nitride films deposited on Silicon (100) substrate at (a) 600^0C (inset: magnified view of AlN (100) peak) and (b) 800^0C (inset: magnified view of AlN (100) peak)

curves obtained for the AlN (100) phase at temperatures of 600^0C and 800^0C are illustrated in Figures 3.2 (a) and (b) respectively. The corresponding crystallite size calculated using the Scherrer formula [38] was found to be 6.12 nm and 2.29 nm in each case respectively. The XRD

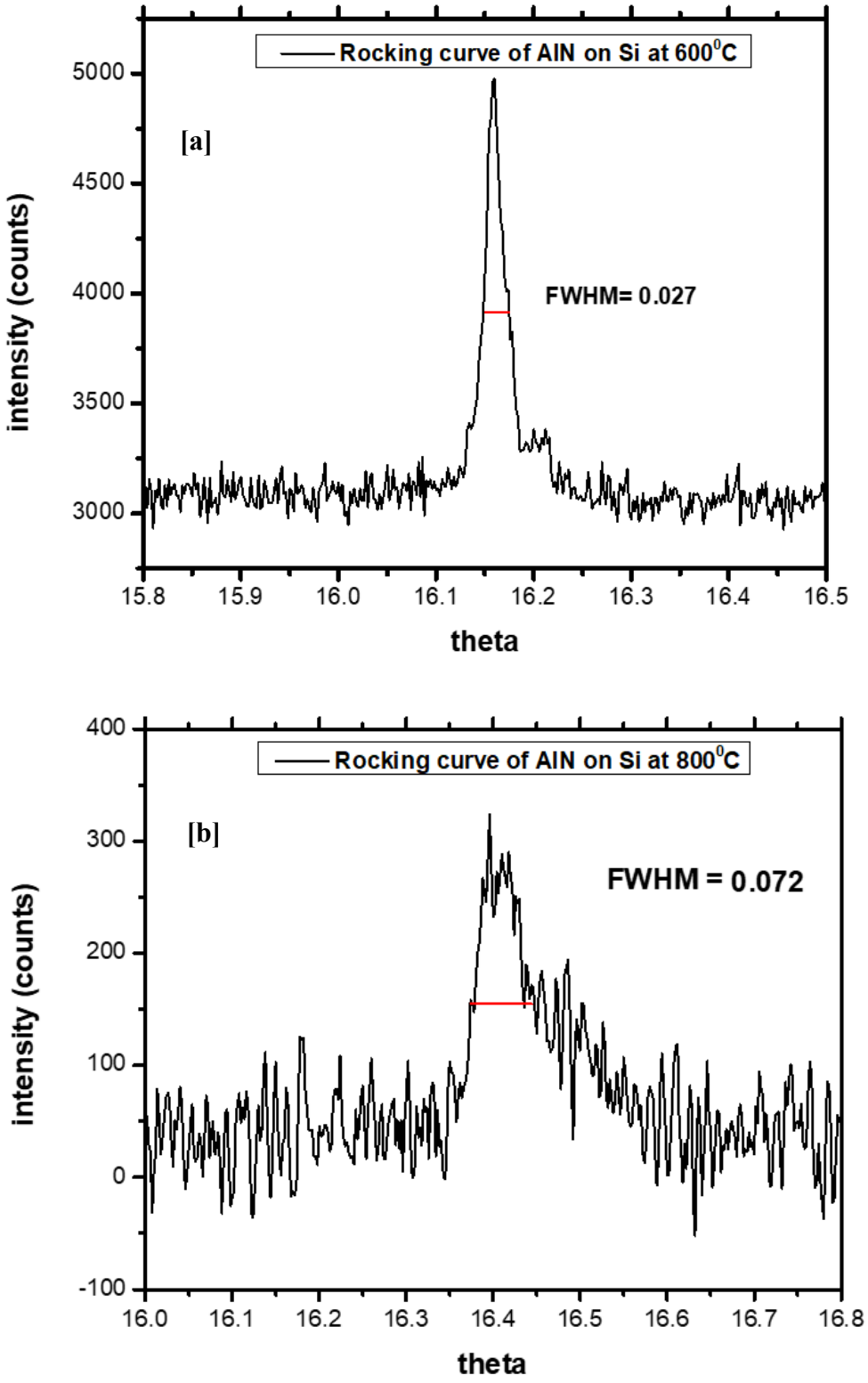

Figure 3.2. Rocking curves and FWHM values obtained for the AlN (100) peak for the films grown at (a) 600^{0}C and (b) 800^{0}C

scans for the AlN films grown on Al_2O_3 (001) substrate at 600^0C and 800^0C are shown in Figure 3.3 (a) and (b) respectively. Both the films show only the dominant substrate peak at 41.8^0. Since

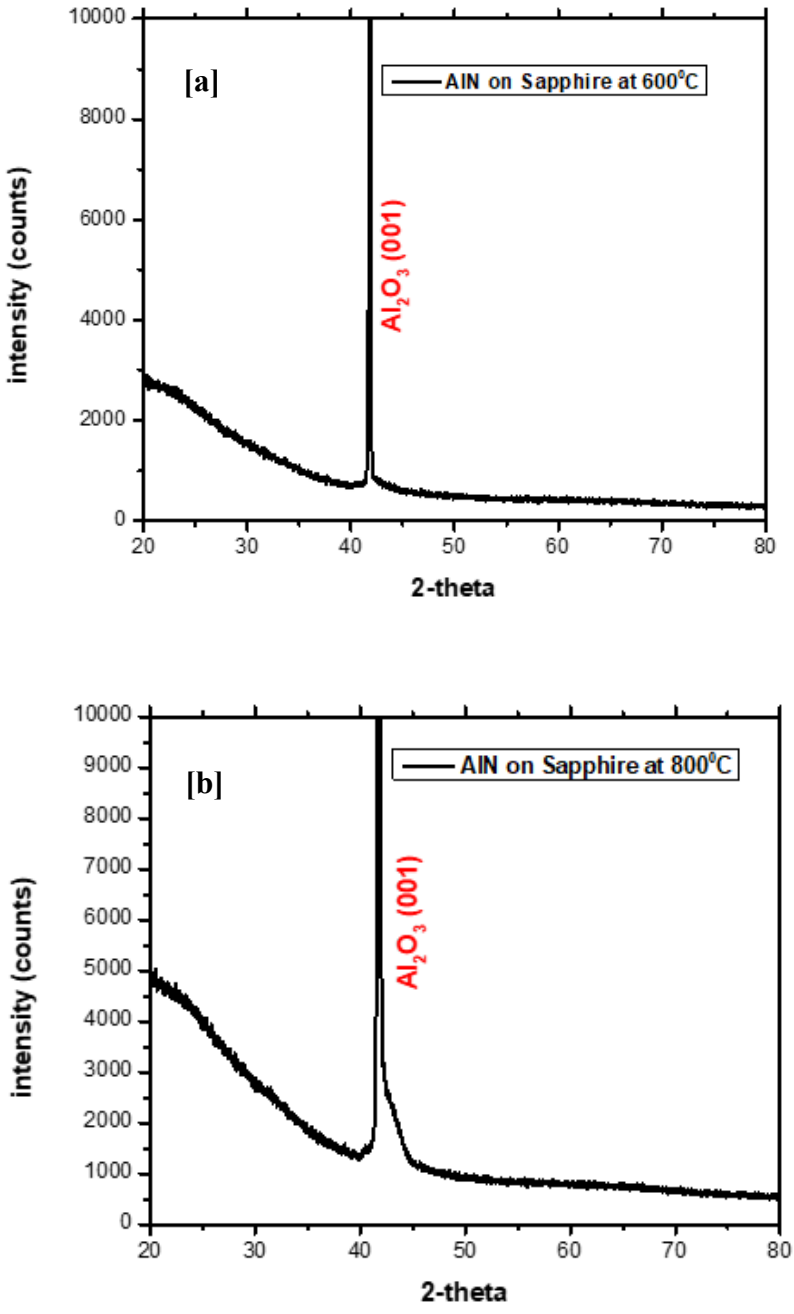

Figure 3.3. XRD results for Aluminum Nitride films deposited on Sapphire substrate at (a) 600^0C and (b) 800^0C

no AlN peaks were observed in either the 600^0C or 800^0C sample even with an extended acquisition time, we performed a Grazing Incidence XRD scan (GIXRD) for the sample grown at 600^0C as shown in Figure 3.4 below. The advantage of such a technique is that the X-Rays penetrate only a shallow depth compared to conventional XRD. Hence, it can be effectively used to get maximum signal from the surface of the film by increasing beam coverage and minimize background scattering from the substrate. For this particular scan, the angle of incidence was fixed at 2^0 with the sample stage being anchored at a particular position while the detector was varied between 8^0 and 80^0. The data reveals an interesting feature in the form of a broad peak around 25^0 which was not present in the previous theta-2theta scans. Khan et al. [39] reports similar broad features obtained during grazing angle scans for magnetron sputtered AlN films grown at 600^0C and associates it with the AlN (002) wurtzite phase.

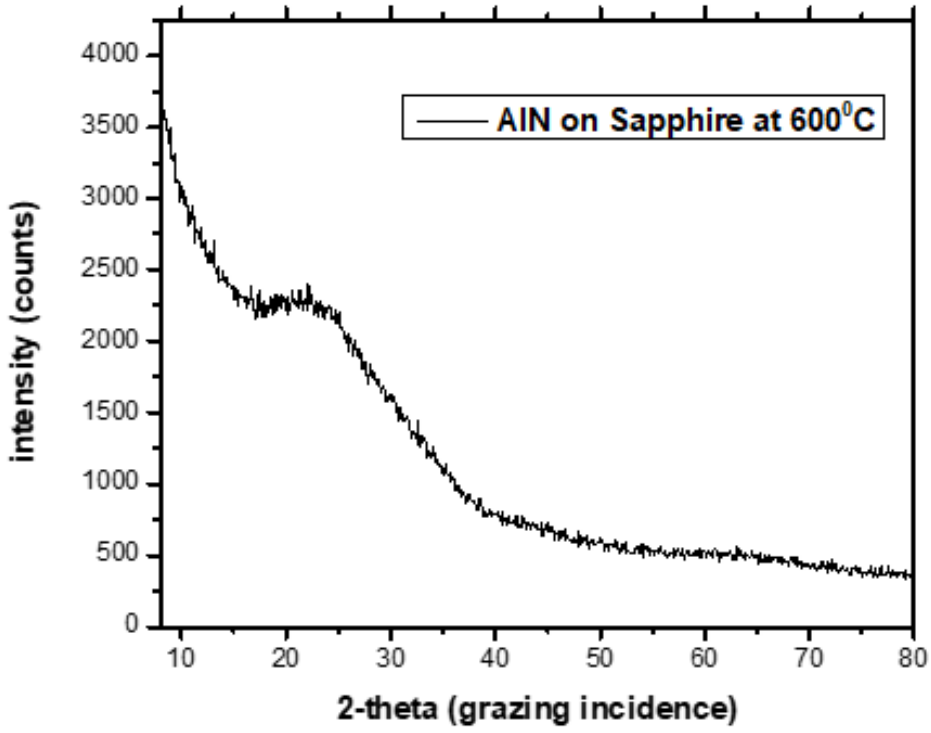

Figure 3.4. Grazing angle XRD scan of Aluminum Nitride film deposited on Sapphire at 600^0C

It is important to note that Aluminum Nitride is hexagonal in structure and hence, four coordinate system of miller indices is necessary to represent the crystal planes without any ambiguity. Therefore, the planes commonly referenced as (001) and (100) are actually (0001) and (10-10) in hexagonal coordinates. One can easily infer from Figure 3.5 below that the (10-10) plane is rectangular while the (0001) plane has a hexagonal symmetry. We must also consider that Silicon is inherently cubic while Al_2O_3 (sapphire) has a hexagonal structure. Combining these two facts helps us in explaining the preferred growth of AlN (10-10) phase on Si (100) and AlN (0001) phase on c-axis oriented, i.e. Al_2O_3 (0001) substrate respectively due to lattice matching. It has been further reported that the wurtzite phase of AlN is composed of two

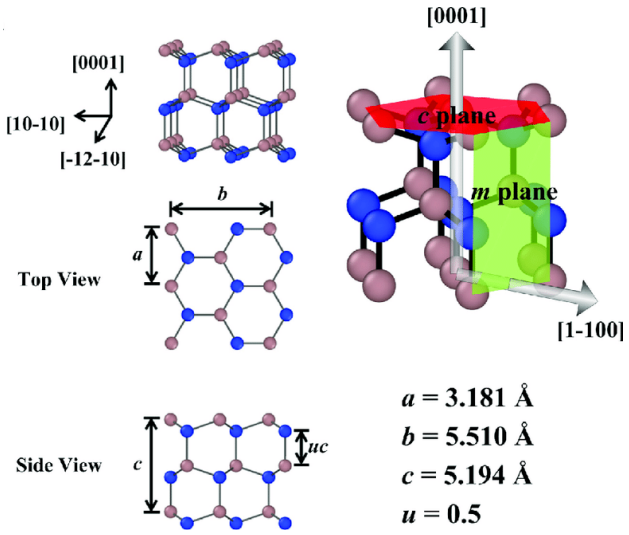

Figure 3.5. Schematic diagram on common growth planes in Wurtzite crystal [40]

distinct kinds of Al-N bonds namely B1 and B2 as shown in Figure 3.6. B1 has lower bond energy and is associated with the plane (10-10) whereas B2 is composed of (0002) and (11-20) planes and requires relatively higher energy. This explains the contrast between the weak, broad

AlN (0002) peak on Al_2O_3 and the sharper AlN (10-10) peak on Si for the films grown at the same deposition temperature, i.e. 600^0C. Further, there is a possibilty that the film on sapphire

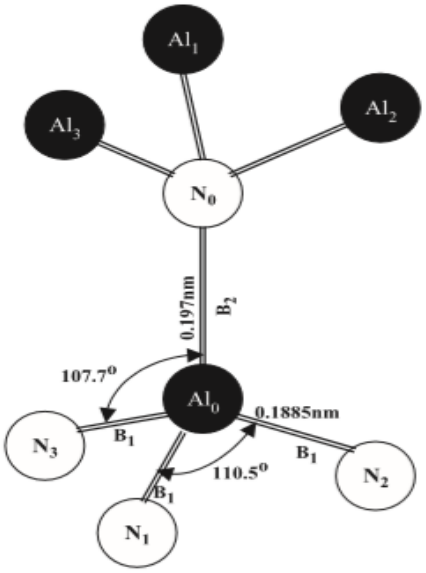

Figure 3.6. Schematic diagram of the wurtzite AlN structure [41]

is either a case of coincident epitaxy or single crystal with misoriented crystal plane as shown in Figure 3.7 (a) and (b) respectively. In case of coincidental epitaxy, two possibilities may arise. In the first scenario, all lattice points of the film coincide with that of the substrate but all substrate

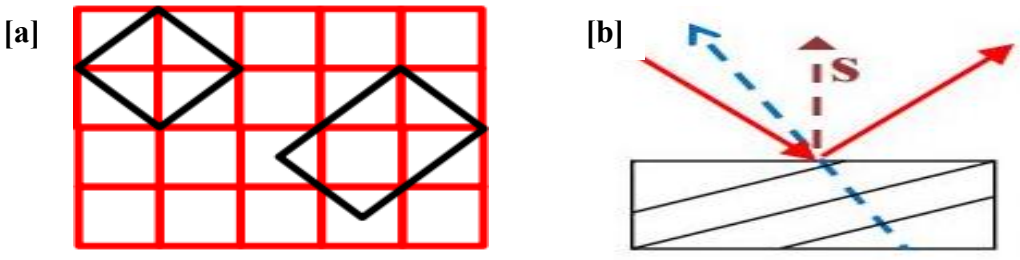

Figure 3.7. (a) schematic example of coincident epitaxial growth indicated by black and red lines for the film and substrate lattices respectively, (b) example of single crystal film with planar misorientation relative to the substrate [42]

lattice points do not coincide with that of the film . In the second scenario, only some of the film lattice points coincide with that of the substrate. In either of these cases discussed above, it is relatively difficult to get a good XRD signal from the film.

3.2 Scanning Electron Microscopy (SEM) and Energy Dispersive X-Ray Spectroscopy

As mentioned earlier during the design test, it cannot be stressed enough that SEM is ostensibly not as good as other surface sensitive instruments like X-Ray Photoelectron Spectroscopy (XPS) while probing films having thickness of the order of a few nanometers. This situation gets further complicated while investigating films grown on insulating substrates like Sapphire, where it is difficult to get a high quality image and a decent EDS spectra simultaneously. Additionally, the bracketing of the Nitrogen and Oxygen peaks in EDS scans continues to be a challenge in our specific case of studying Alumium Nitride.

Due to the relative ease of imaging, we start our investigations with the films grown on Silicon substrates. Figure 3.8 shows a micrograph SEM image of the AlN film grown on Silicon at 600^0C. The image reveals that the film contains some artifacts on a predominantly smooth surface. Upon close examination, these features appear to be nodules interspersed on the flat bed. A magnified view of such a nodule pair is presented in Figure 3.9 (a) below. In order to inspect the composition of the nodule, we perform a line scan that stretches between the film regions on either side and intersects the nodules in the middle. As expected, the line scans indicate that the nodules are composed of Aluminum Nitride. The individual atomic percentages of Aluminum, Nitrogen and Silicon relative to the stored X-ray database of the elements, stored in the EDS software is shown in Figure 3.9 (b), (c) and (d) respectively. It is clear from the figure that the Aluminum and Nitrogen lines follow a similar trend across the nodules signifying the

correlation between them. The Silicon line displays a complementary trend and is maximum in the interlying regions of the film where no nodules are present, due to more signal count from the substrate. The most notable feature however, is the non-zero intensity of the Aluminum and Nitrogen lines on the regions where nodules are absent. This helps in corroborating our assumption that in addition to the nodules, we have a film that is composed of Aluminum Nitride, which is our primary goal. In order to investigate this further, we perform EDS scans on the film as well as on the nodule and make an effort to compare the two spectras as shown in

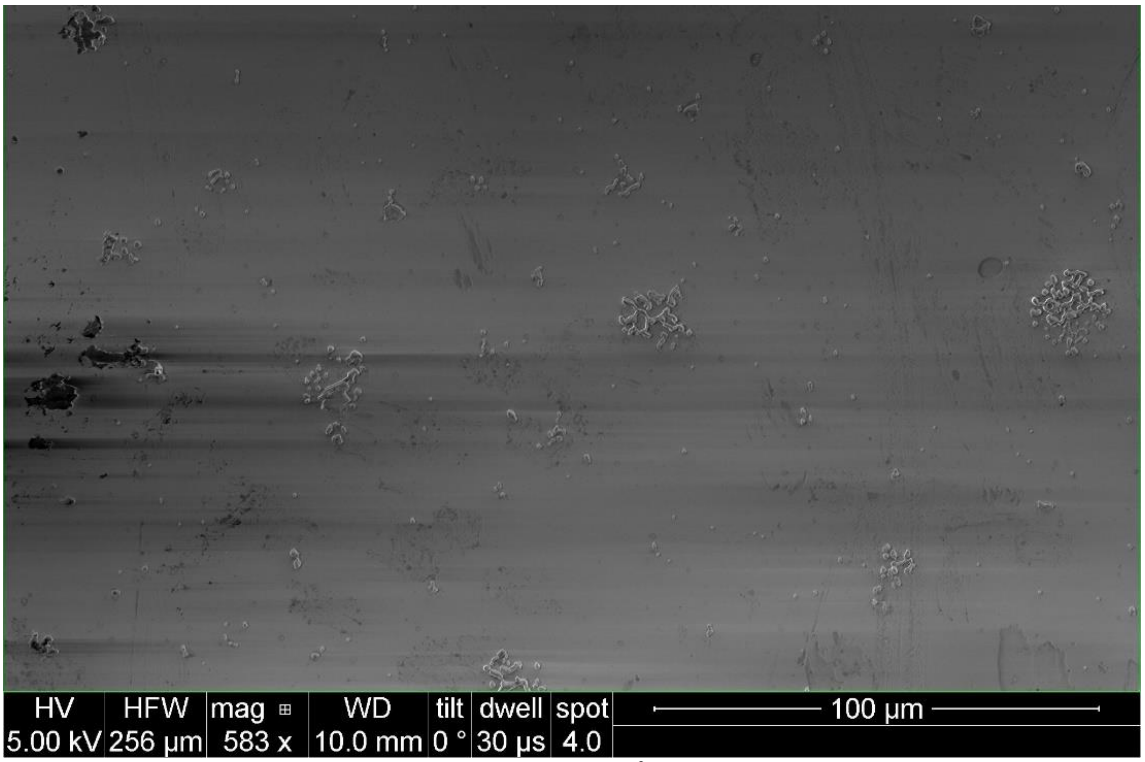

Figure 3.8. SEM image of AlN film on Silicon at 600^0C

Figures 3.11 (a) and (b) respectively. We observe a sharp Aluminum and Nitrogen peak on the nodules while the film shows a much weaker signal for Nitrogen. This is understood by

visualizing the fact that the nodules are 3D projections on the film surface and thus the effect of background signal is significantly less as compared to on the film. Thus, special measures are

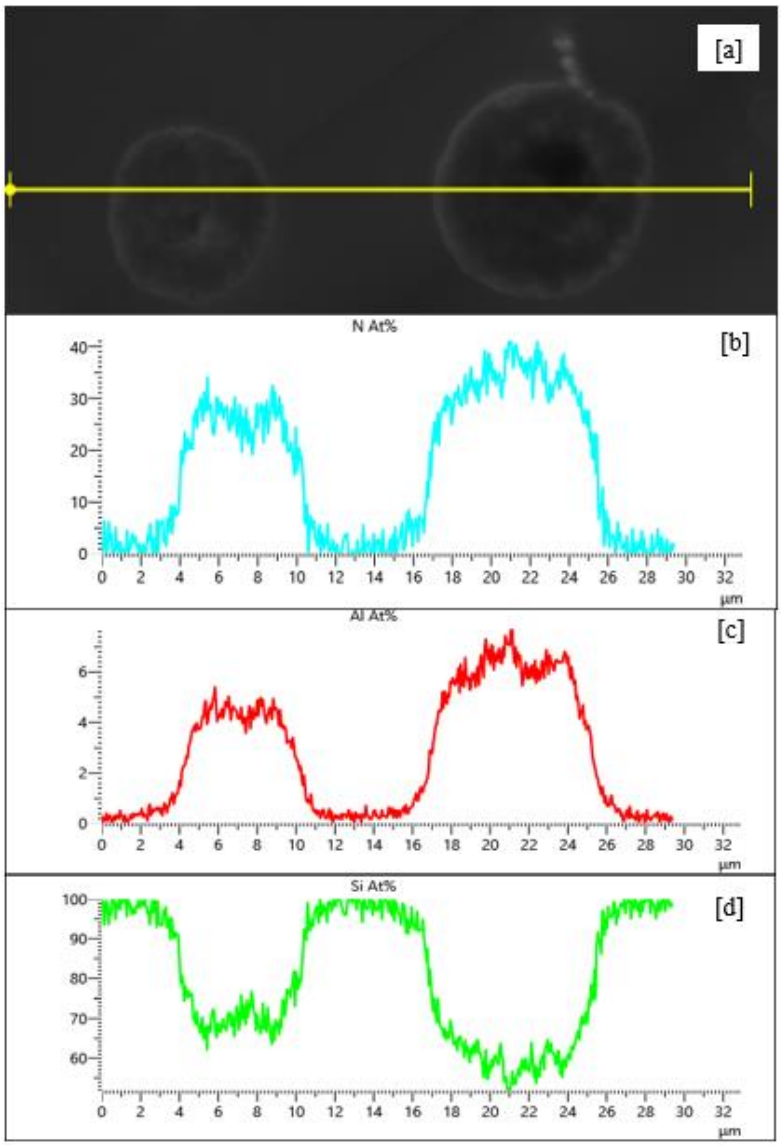

Figure 3.9. (a) Magnified view of AlN nodule on Si at 600^0C, Line scan atomic weight percentage data for (a) Nitrogen, (b) Aluminum and (c) Silicon

necessary to extract the best Nitrogen signal and pull it above the noise level. In order to achieve this, we perform an elaborate elimination process by including two more EDS spectras in our

calculations, i.e (1) bare Silicon substrate and (2) Aluminum film on Silicon without any Nitrogen. We begin by normalizing the Silicon peaks to the same intensity on all four spectras. Next we substract the Silicon signal from the other three. After the Silicon signal has been successfully elinated, we now normalize the Aluminum peak to the same intensity on the three remaining spectras. In the final step, we substract the Aluminum signal from the remaining two spectras and plot them on the same graph. Figure 3.10 shows the normalized background substracted EDS data for the AlN nodule and film on the same graph. The Nitrogen peak is much more pronounced in this processed data and supports the assumptions we made during the line scan analysis. Since the signals are all the results of the interactions between the electron beam with the sample, the coexistance of the Al and Ni from the EDS signals provides the necessary evidence for the presence of Aluminum Nitride film.

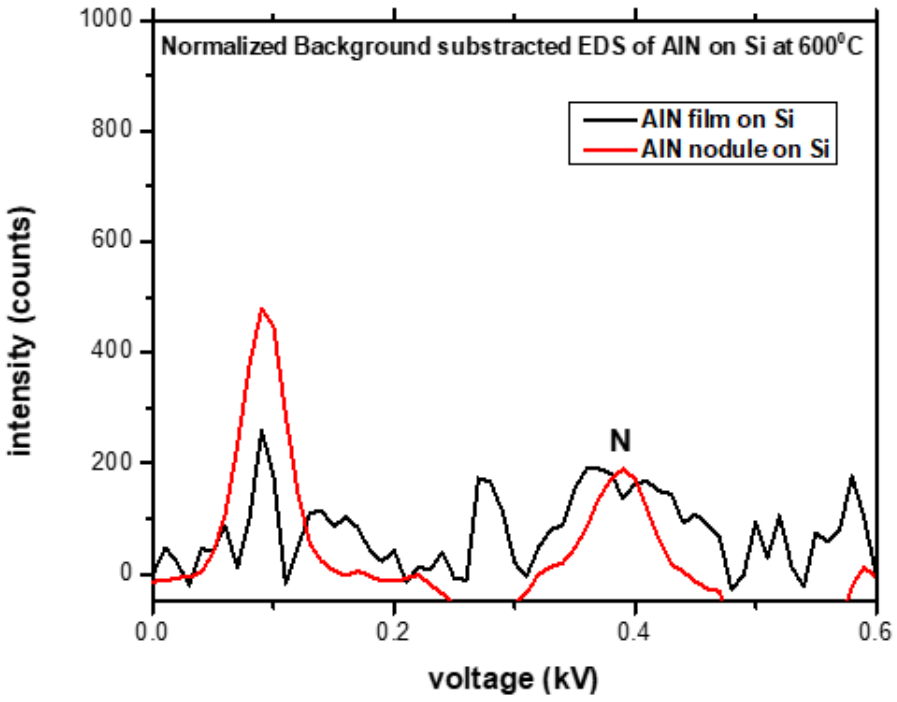

Figure 3.10. Normalized and background subtracted EDS data of AlN on Si at 600^{0}C

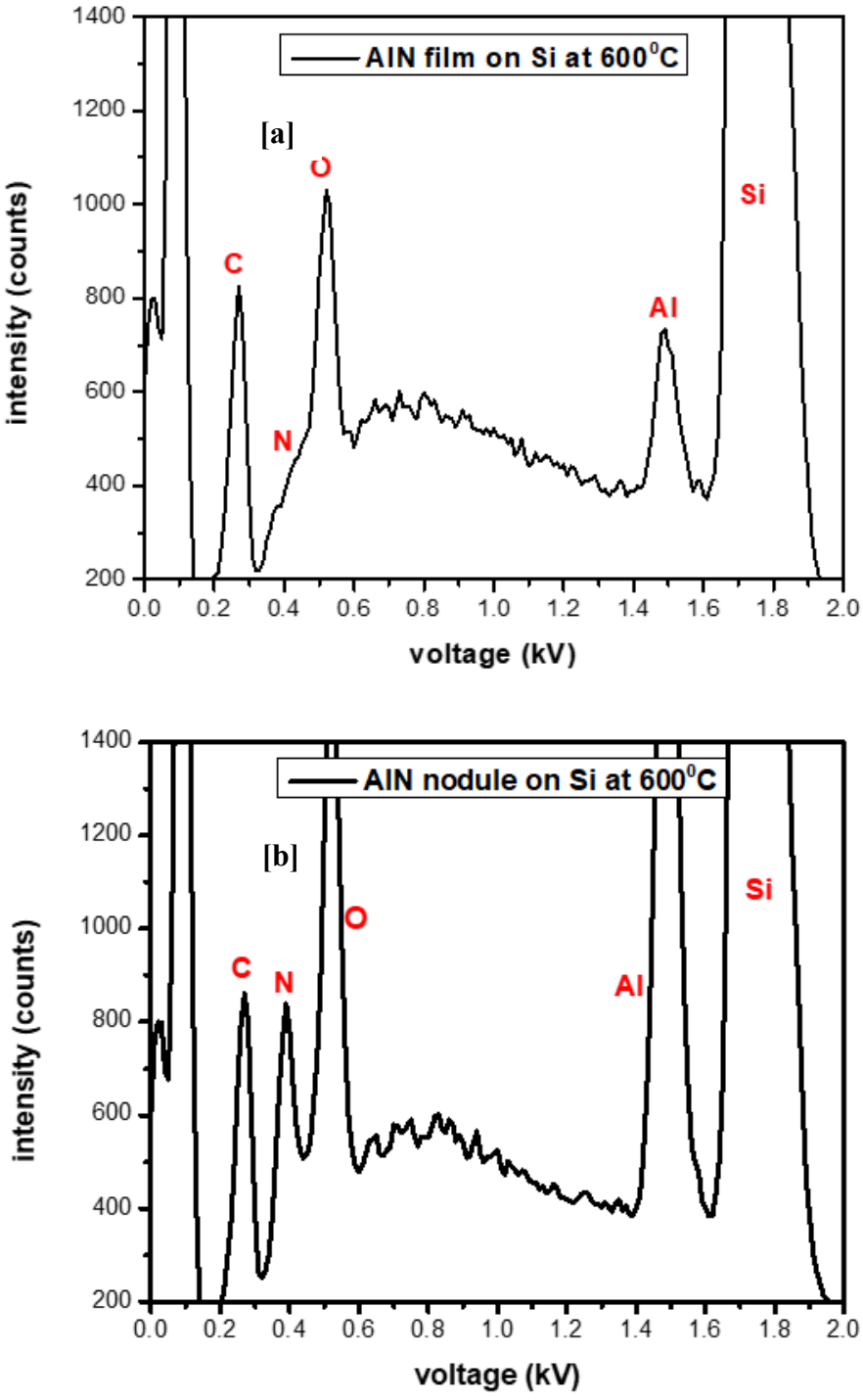

Figure 3.11. EDS spectra of (a) AlN film on Si at 600^{0}C and (b) AlN nodule on Si at 600^{0}C

The AlN film deposited on Silicon at 800^0C exhibits similar characteristics as the 600^0C sample. Figure 3.12 (a) shows the mapped area of a single AlN nodule on the film surface. EDS Mapping analysis performed on the nodule clearly indicates Al-Kα and N- Kα emissions as shown in Figure 3.12 below. The SEM micrograph and line scans for the mapped nodule is shown in Figure 3.13 below. Once again, the Aluminum and Nitrogen lines show a similar trend by following each other while the Silicon peak complements it. Further, the EDS spectra

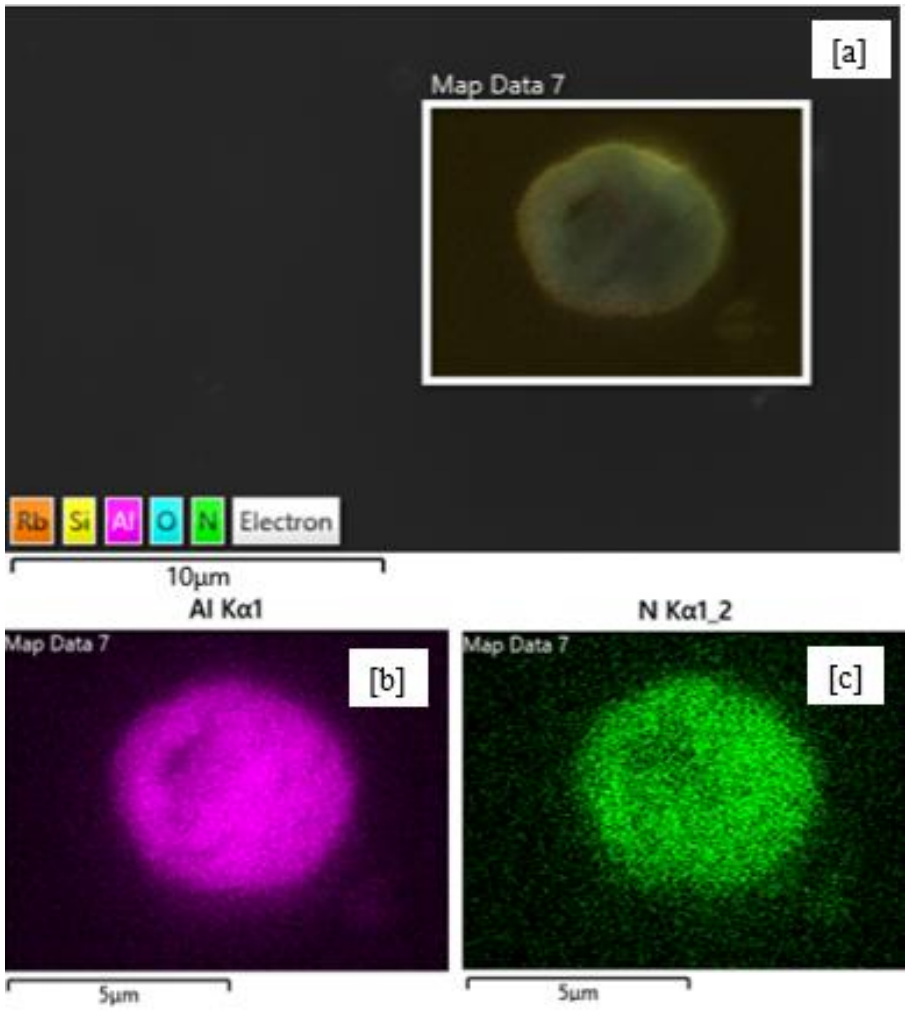

Figure 3.12. (a) Area map showing AlN nodule on Si at 800^0C, Mapping data on the AlN nodule revealing (b) Aluminum Kα emission, (c) Nitrogen Kα emission

obtained for the film as shown in Figure 3.14 clearly indicates the presence of Aluminum and

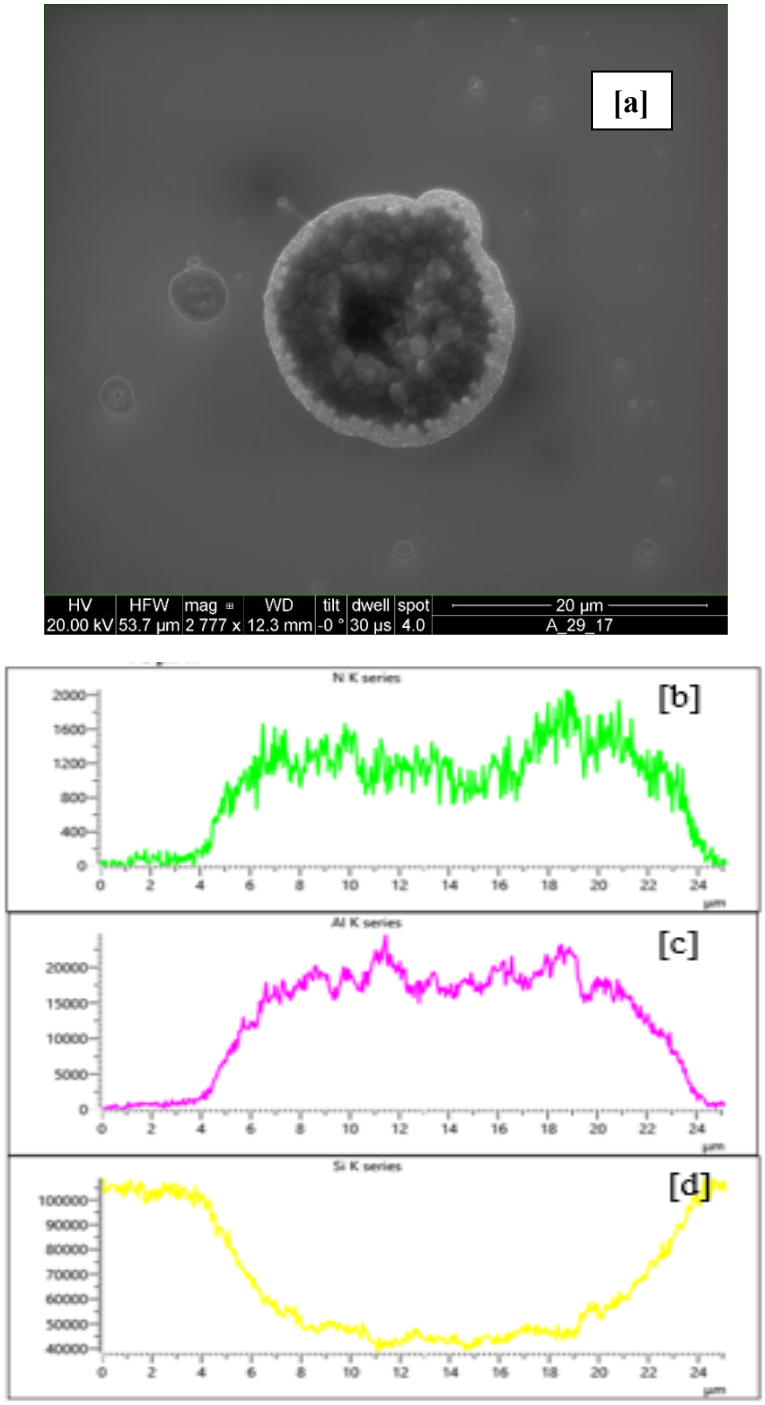

Figure 3.13. (a) SEM micrograph of AlN nodule on Si at 800^0C, Line scan data showing X-ray counts from EDS attributed to (b) Nitrogen, (c) Aluminum and (d) Silicon

Nitrogen peaks confirming Nitride formation. Thus, we have gathered enough evidence to show that we have successfully grown an Aluminum Nitride film on Silicon at 600^0C as well as 800^0C.

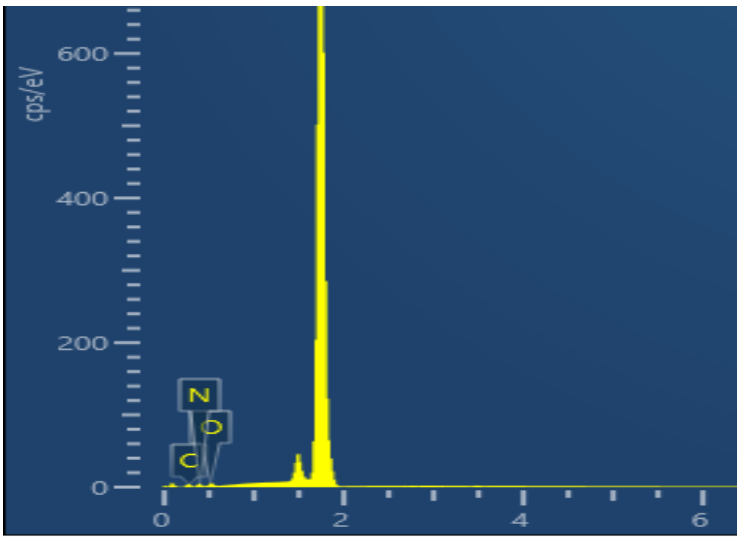

Figure 3.14. EDS spectra of AlN film on Silicon at 800^0C

The EDS spectra of AlN film on Sapphire (Al_2O_3) grown at 600^0C is shown in Figure 3.15 below. As explained earlier, due to the insulating nature of the Sapphire substrate, imaging is a real challenge. At higher magnifications, the occurrence of charge build up due to poor conduction of electrons is almost unavoidable even when a copper tape is used to make a conductive path between the film and the sample stage. This results in blurred poor quality images. However, the EDS scan shows a sharp Aluminum peak and a shoulder Nitrogen peak next to the Oxygen line. Although the huge Oxygen peak from the Al_2O_3 substrate almost serves to mask the Nitrogen line, yet the combined Al and Ni peak features are just sufficient enough so that we can satisfactorily present the evidence of an Aluminum Nitride film.

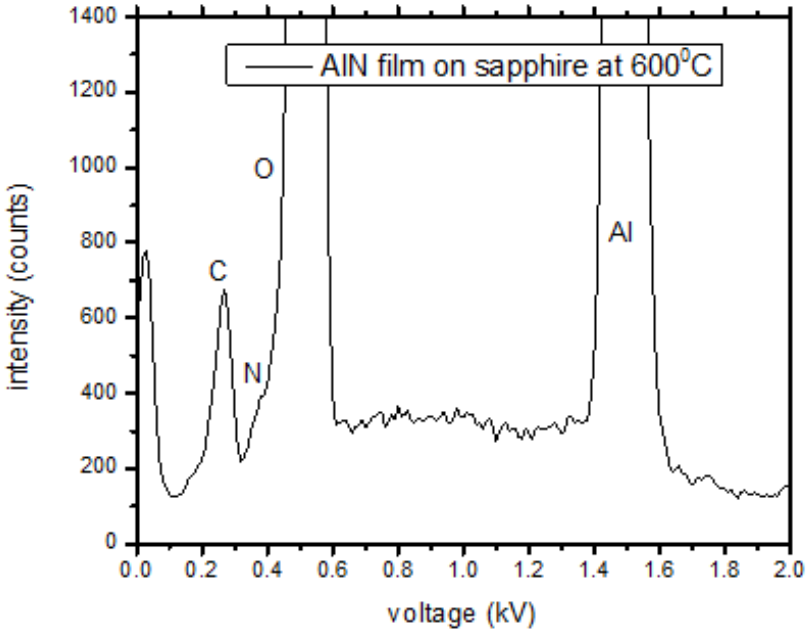

Figure 3.15. EDS spectra of AlN film on Sapphire at 600^{0}C

3.3 Profilometry

We use the Dektak profilometer to analyze the thickness of the as-grown films. In order to do this, we chose the un-deposited regions of the substrate as the reference point for measurements. For the films grown on Silicon, this was easily achieved by selecting the regions masked by the clips on the substrate holder as can be seen from Figure 3.16. On Sapphire

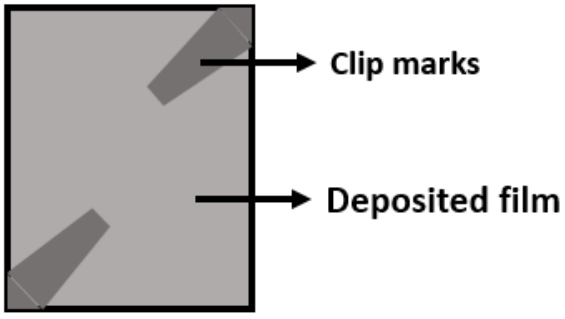

Figure 3.16. Graphical representation delineating clip marks and film on Silicon substrate

however, it was difficult to delineate the deposited and un-deposited regions due to the transparent nature of the substrate. Hence, only the thickness measurements performed on films grown on Silicon substrates are presented in this section.

Figures 3.17 (a) and (b) show the film thickness recorded for AlN films grown at 600^0C and 800^0C respectively. As the profilometer tip is rastered across the film surface, both films

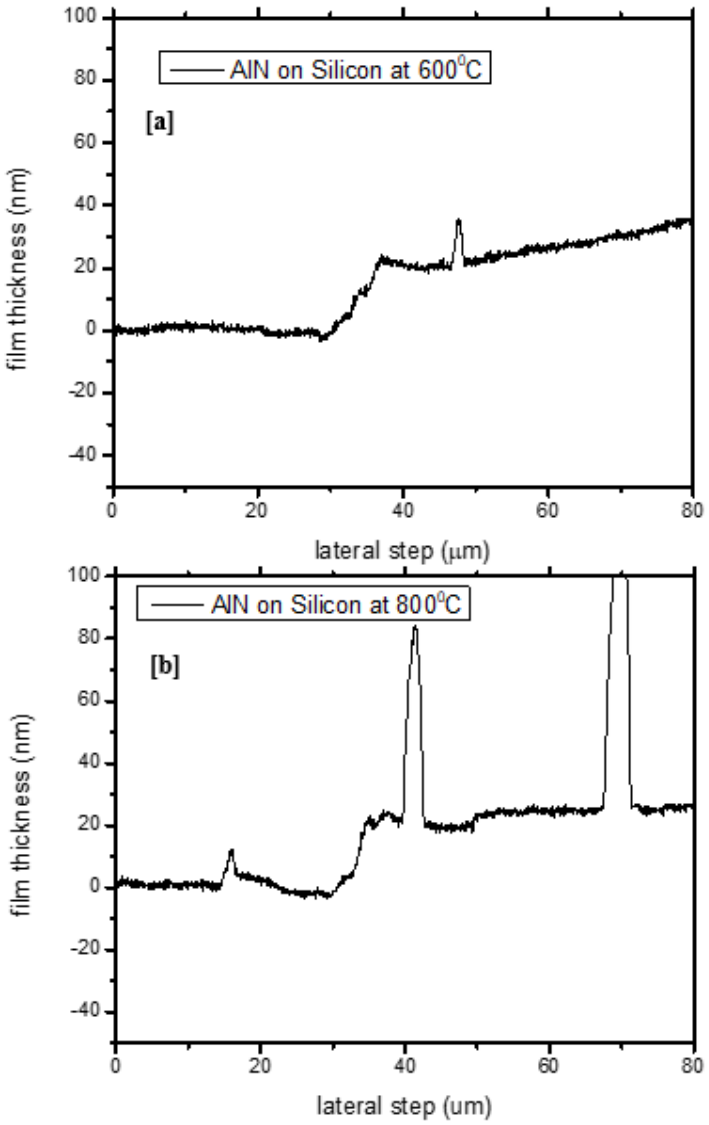

Figure 3.17. Profilometer data for AlN film on Silicon deposited at (a) 600^0C and (b) 800^0C

show a clear step from the mask that remains reasonably flat with the exception of a few hills, especially on the 800^0C sample. The thickness on both the samples was found to be 20nm $\pm$ 5%. Table 3.1 enlists the film thickness of a selected number of our previous films grown at different deposition parameters in addition to the latest ones. The thickness of the films vary between 20-50 nm $\pm$ 5%. For the films having the same number of laser shots, the film thickness was found

Table 3.1 Film thickness as a function of deposition parameters

Sample	Annealing	Duration of Growth (No. of laser pulses)	Film thickness (nm)
Al on Si without gas at RT	None	5,000	20 $\pm$ 5%
Ni on Si (PLD +CVD) at RT	None	5,000	50 $\pm$ 5%
AlN on Si (PLD+CVD) at 600^0C	None	24,000	40 $\pm$ 5%
AlN on Si (PLD+CVD) at 600^0C (annealed)	Post Growth	24,000	20 $\pm$ 5%
AlN on Si (PLD+CVD) at 800^0C (annealed)	Post growth	24,000	20 $\pm$ 5%

to be lesser in the ones that were annealed post deposition. Further, it was observed that the thickness was less in the films grown at elevated temperatures even though the number of laser shots were significantly higher in the latter. This is because at higher temperatures, the mobility of the surface ad-atoms promote epitaxial tendency for the films. [43] Although the Aluminum and Nickel film grown at room temperatures have the same number of shots, the difference in thickness can be related to the difference in ambient pressure during deposition. It has been found that the emission rate of Nickel increases with ambient pressure in the 10^{-6}-10^{-2} range. [44]

Since the Ni film was grown in laser assisted CVD mode with ambient pressures in the range of 10^{-2} torr, the thickness is relatively higher than that of Aluminum film grown by simple PLD. Thus, the profilometer data confirms that the quality of our films improved with temperature and annealing as per expectation.

3.4 Atomic Force Microscopy

Figure 3.18 shows a 5µm × 5µm topographical survey of the AlN film on Silicon grown at 600^0C. The image reveals distinct regions of film growth which are clearly islands with sharp edges as can be seen from the contrast in the image. In order to investigate the step height of these features, we use ImageJ to perform a profile scan along a line intersecting the

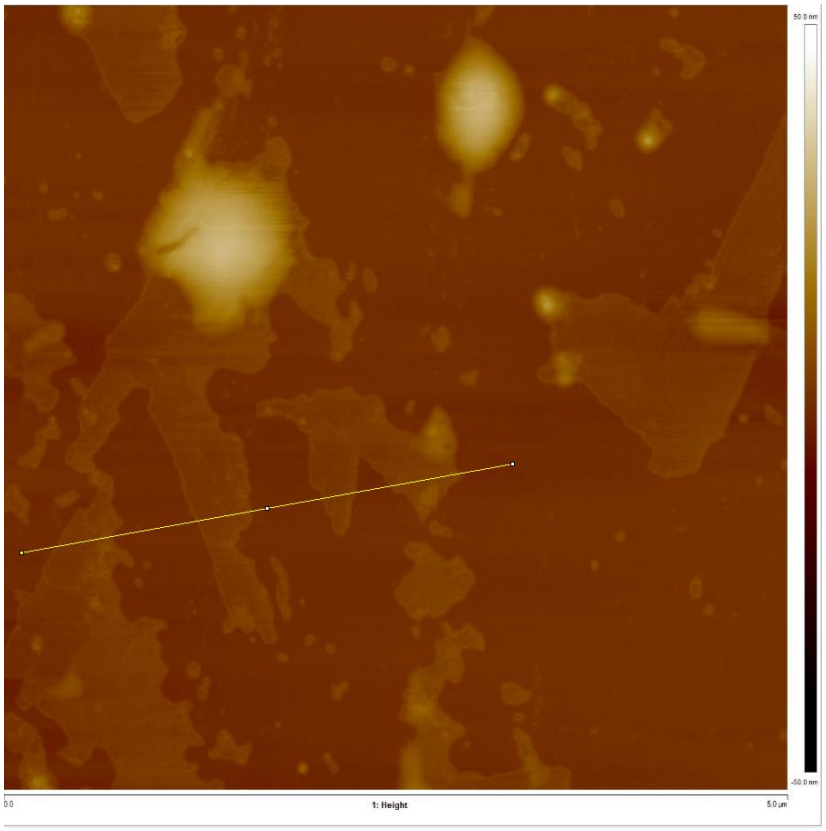

Figure 3.18. AFM topographical survey of AlN film on Silicon deposited at 600^0C

islands. As can be seen from Figure 3.19, we observe multiple steps each with a height of 10 gray bits above the reference. In order to get the exact step height, we first calculate the height per gray bit resolution by dividing the vertical scale of the image, i.e. 100nm by the total number of pixels, i.e. 256 for an 8-bit image. Next, we multiply the step height in gray bits by this resolution. Following this process, we obtain a step height of 3.9 nm. Further, the number of

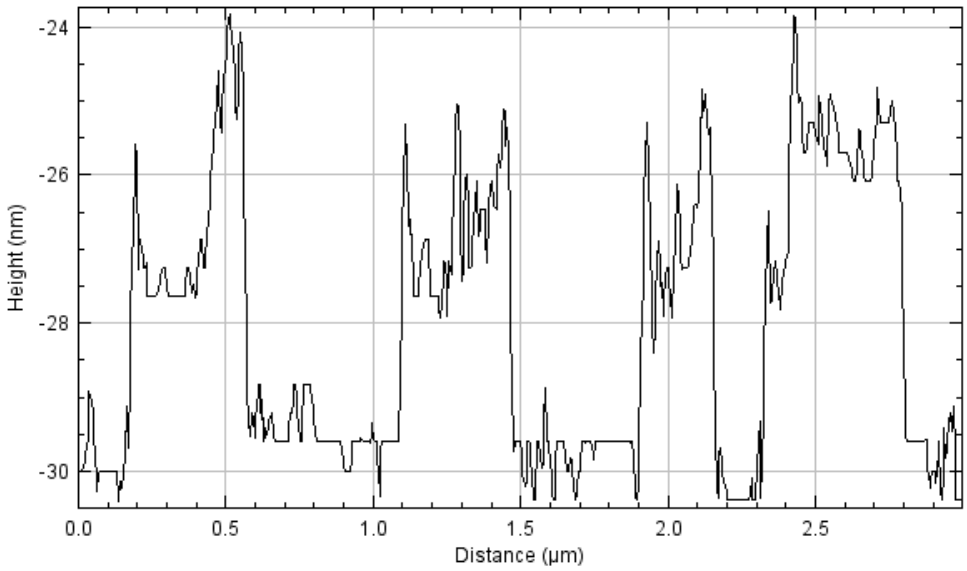

Figure 3.19. Profile plot of AlN film islands on Silicon substrate performed using ImageJ

steps in the profile scan match the number of intercepts in the line scan confirming our initial assumptions. We also observe two bold features towards the upper left and right side of the image. The profile scan across these features shown in Figure 3.20 indicates that they have a step height of 39 nm inviting the possibility that they are droplets of Aluminum. Although droplets are undesirable in any form of film growth, we notice two interesting features that are worth mentioning. Firstly, the density of the droplets is significantly less as compared to the film. Secondly, it appears that that some of the droplets may have got nitrided and acted as a source of film growth. In order to further understand the growth mechanism, we explore the common

modes of thin film growth as illustrated in Figure 3.21. As described by the figure, the growth modes can either be layer by layer, island formation or a combination of layer and islands. Since, we have already observed islands in the image, the possibility of layer by layer growth can be eliminated. This is further confirmed by the fact that the step height of an AlN monolayer is approximately 2 angstroms [45], whereas, in our case the step heights are 40 angstroms. This leads us to consider the next possibility. Upon close inspection of Figure 3.18, we observe the presence of finer regions of contrast shown by the image. It could be possible that the regions underlying the islands are composed of finer films. If the films could be characterized in-situ, it

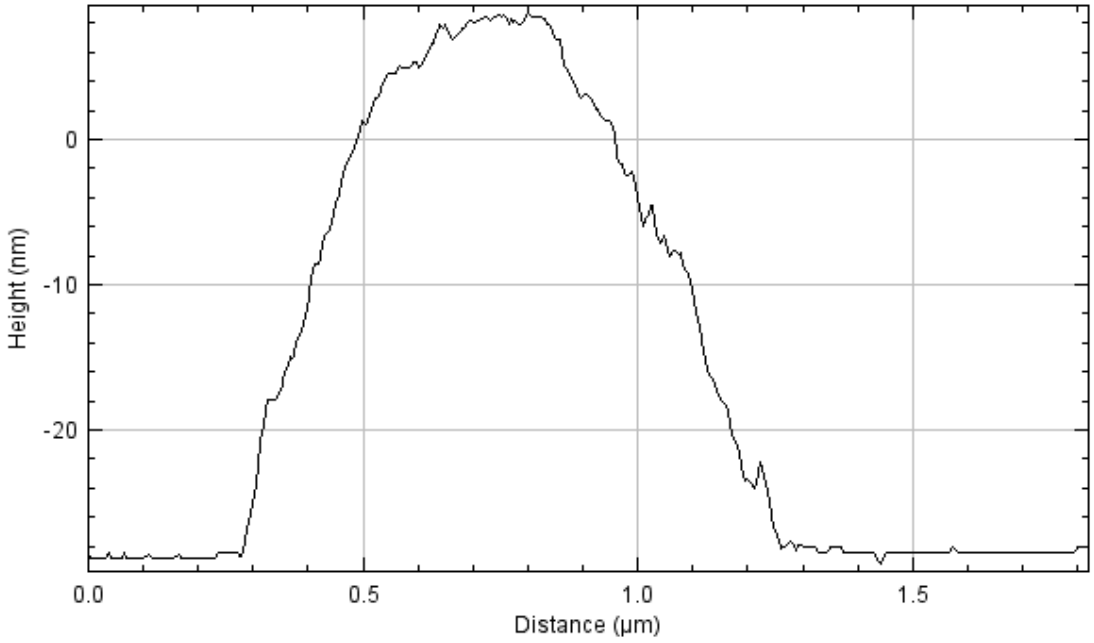

Figure 3.20. Profile plot of Al droplet on Silicon substrate performed using ImageJ

would allow as to better understand the growth mechanism step by step. Unfortunately, this evolution cannot be fully realized in ex-situ imaging. Therefore, at this stage there is no conclusive evidence whether those regions are the substrate or contain finer films. Thus, the most

logical argument is that we have a combination of islands as well as film. Zhang et al. [46] reports an interesting mechanism where growth first starts with a 2D SnS_2 mechanism to form islands. These islands coalesce until layer closure is attained. Following this step, SnS_2 mechanism takes over and starts forming 3D islands at the grain boundaries. Thus, there is this continuous competition between the energetics of layer formation as well as minimizing the surface energy until one of the processes dominate.

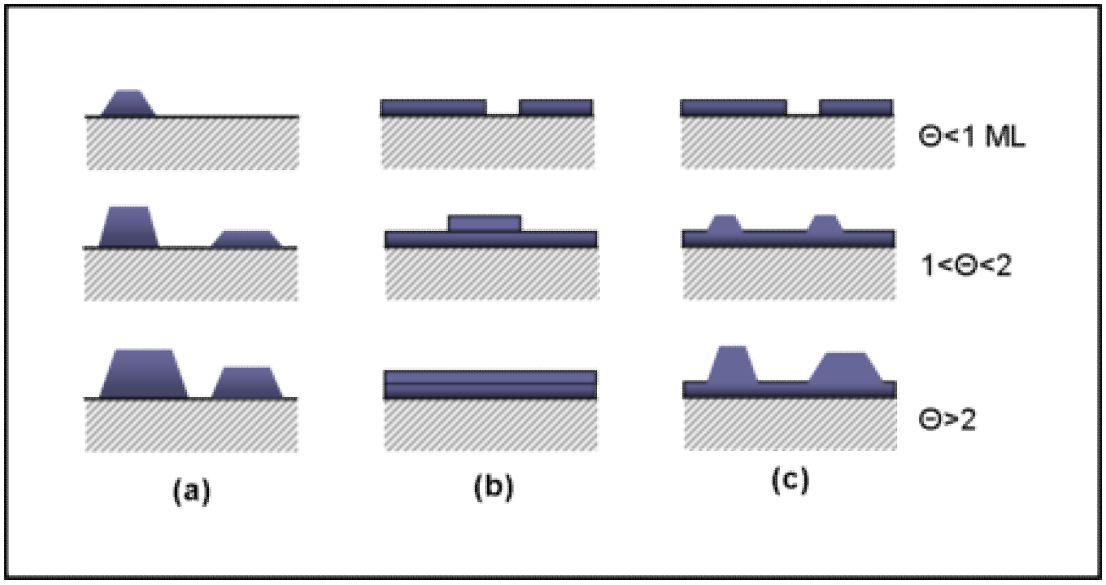

Figure 3.21. Cross sectional views of primary modes of film growth including (a) Volmer-Weber (island formation), (b) Frank–van der Merwe (layer by layer), and (c) Stranski-Krastanov (layer plus island) [47]

Next, we investigate the film grown on Sapphire from the topological survey image shown in Figure 3.22. Unlike the films grown on Silicon, no large islands are present. However, it is clear that small plateaus of film regions are distributed throughout the surface. To further understand the morphology, we analyze the profile plot as shown in figure 3.23 and calculate the average step height to be 1.2 nm. This is relatively less than the films grown on Silicon. However, there appears to be some roughness in the profile of the film. The variation in surface

roughness with number of process steps for AlN film growth on Sapphire was studied and reported by Ambartsumov et al.[48] He observed that the roughness increased linearly with the number of process steps. However, although we see features very similar to the films deposited by his group, the roughness of our films lie in an intermediate range between the best and worst films reported by him. From the profile plot shown below, we observe that the number of steps across a 500 nm lateral scan is approximately eight which is not as bad as we predicted. Thus, it is reasonable to say that the film growth on Sapphire appears to be more uniform but the nodules

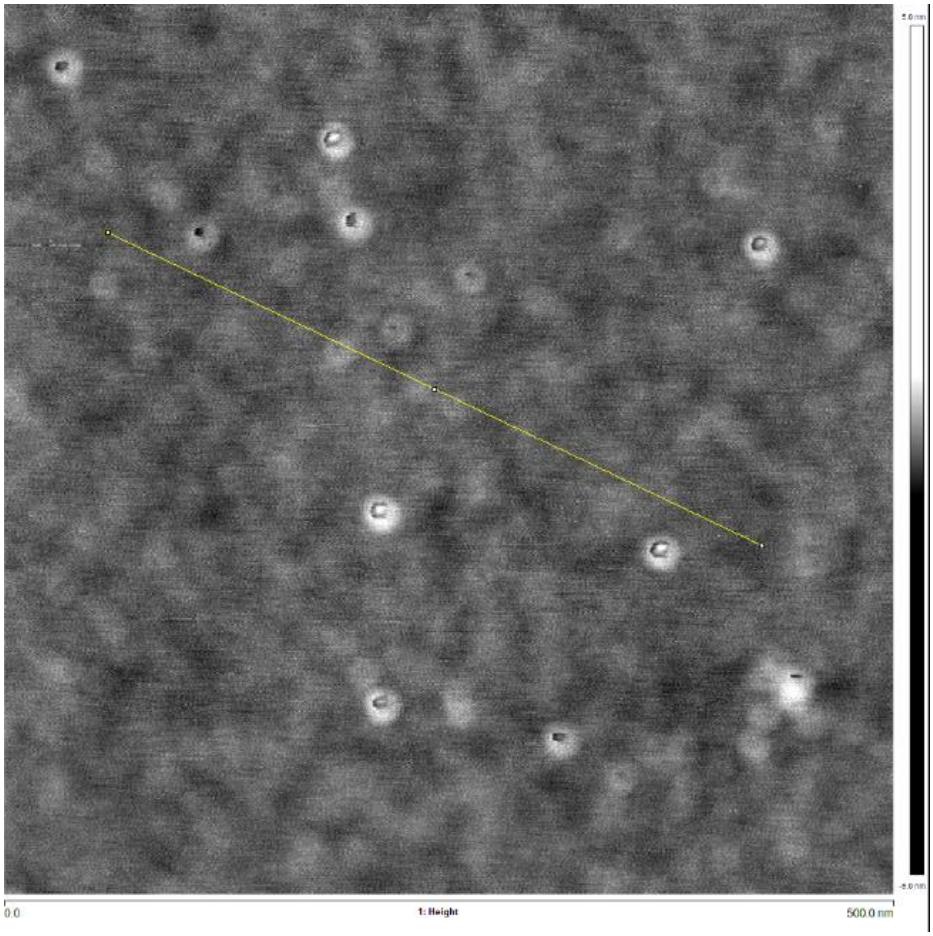

Figure 3.22. AFM topographical survey of AlN film on Sapphire deposited at 600^0C

are not as large and flat as in Silicon . Thus the film is compromised in terms of crystallinity and smoothness.

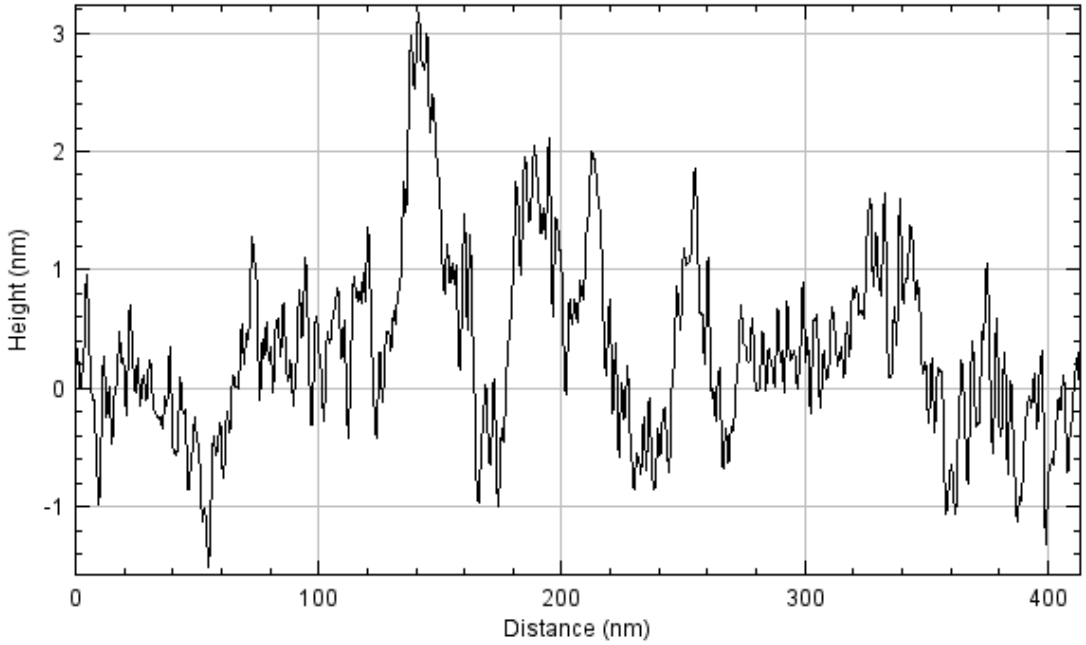

Figure 3.23. Profile plot of AlN film on Sapphire substrate performed using ImageJ

3.5 Raman Spectroscopy

In this section we present the Raman data for two of our films, i.e. AlN on Silicon at 600^0C and AlN on Al_2O_3 at 600^0C. In order to minimize instrumental errors during data acquisition, a zero calibration was done followed by peak calibration with respect to standard Silicon substrate peak having a wave number of 520.7cm^{-1}. All spectra were acquired using a 50x microscope objective and a d0.3 ND optical filter.

Figure 3.16 shows the Raman spectra of AlN film on Silicon deposited at 600^0C. We observe the presence of the dominant Silicon substrate peak at 521cm^{-1} with the addition of Silicon overtones at 618 $cm^{-1,}$ 942cm^{-1}, 957cm^{-1} and 977cm^{-1} respectively. The characteristic

Raman peak for AlN is approximately 660 cm^{-1} and corresponds to the E_2 (high) according to literature. However, in our data we observe a weak and shifted peak at 683 cm^{-1}. According to Kallel et al. [49], this is due to compressive stress in the film due to lattice mismatch with the substrate. He further explains that since the E_2 (high) mode is most pronounced in c-axis oriented Wurtzite AlN, it is highly sensitive to the substrate and can be either under tensile or compressive stress depending on the degree of lattice mismatch. Also, recalling from the discussions in our XRD section, we have seen that the AlN film grown on Silicon has a single (100) crystalline phase which is different from its c-axis oriented (001) phase. Thus, the direct correlation between the crystalline phase of AlN and the sharpness and position of the E_2 peak helps explain the peak shift in our data.

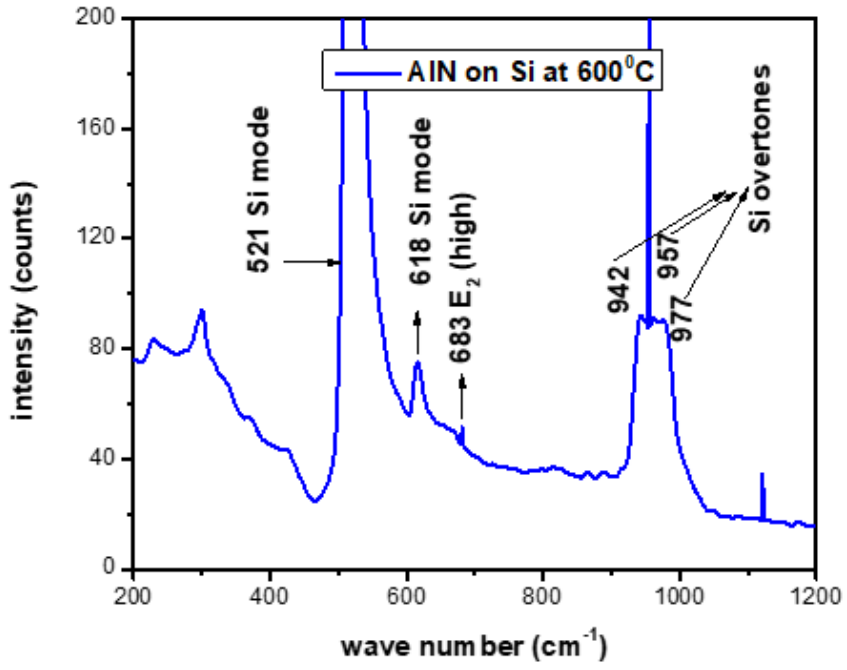

Figure 3.24. Raman spectra of AlN on Si at 600^0C

The Raman spectra for AlN on Al_2O_3 is illustrated in Figure 3.17 below. The peaks at 418 cm^{-1}, 576 cm^{-1} and 750 cm^{-1} can be attributed to the Sapphire (Al_2O_3) substrate. Further investigation reveals that the E_2 peak although weak is fairly accurate at 661 cm^{-1}. We also observe the emergence of the A_1 (LO) mode at 863 cm^{-1} previously unobserved in the film grown on Silicon. Since, the A_1 mode is a strong signature of the c-axis oriented Wurtzite phase, it confirms the growth of c-axis oriented film on Sapphire. However, the peak broadening of the

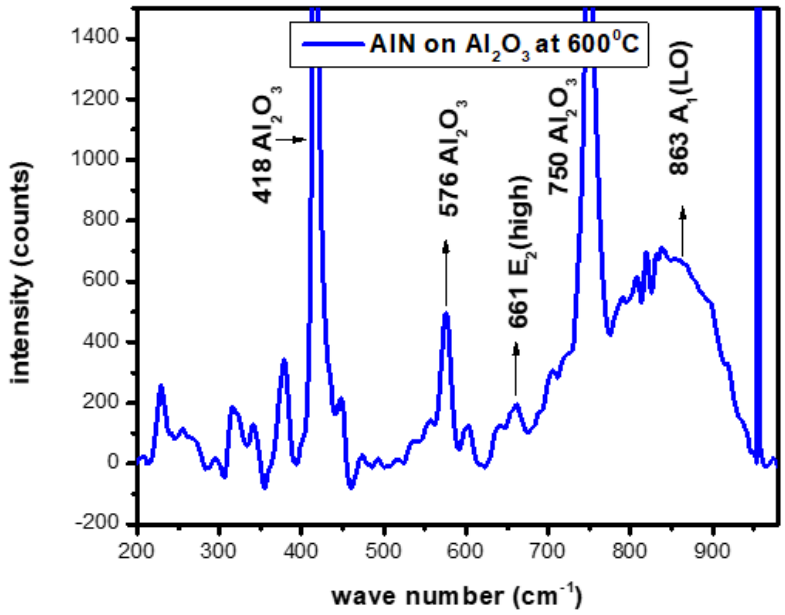

Figure 3.25 Raman spectra of AlN on Al_2O_3 at 600^0C

A_1 mode is indicative of defects in the film. [50] This is in agreement with our XRD and AFM data and suggests that although the growth on Sapphire is relatively better in terms of phase matching, it is not continuous and is marked by regional inconsistencies due to the distributed presence of nodules across the sample.

SUMMARY AND FUTURE WORK

We have been successful in developing a CVD assisted PLD system for the department that is cleaner than existing deposition tools and free from contaminants. Through extensive testing of process parameters, we have been able to optimize the system for growing metal nitrides as a proof of concept. By employing an array of characterization techniques like XRD, AFM, SEM, EDS and Raman Spectroscopy we were able to confirm the superior quality of the deposited films as compared to traditional PLD systems. Although the process parameters may vary depending on the type of films to be grown, we have been able to demonstrate that this new chamber is ready to be used as a platform for growing novel materials. We are enthusiastic that this system will be a great addition to the department in terms of materials research, particularly with respect to exploring the properties of 2D materials.

In order to understand the film growth mechanism during the process and for better controllability, we require in-situ characterization techniques. With respect to Aluminum Nitride films in particular, we need to install a mass spectrometer to study the dynamics of laser-gas-plume interaction. Although we have significantly less number of droplets in our films, the inclusion of screens could further enhance the film quality. As we have already shown in our discussions that annealing improves the film quality, there is scope of improvement in terms of finding the best annealing parameters. Last but not the least, better methods of substrate preparation need to be formulated as we know that it highly dictates the film characteristics. Thus, by achieving these future goals, we would be able to further optimize our system and realize its full potential.

REFERENCES

1. O'Hanlon, J. F. Advances in Vacuum Contamination Control for Electronic Materials Processing. *Journal of Vacuum Science & Technology A: Vacuum, Surfaces, and Films* **1987**, *5*, 2067–2072.

2. Cooper, D. W. Particulate Contamination and Microelectronics Manufacturing: An Introduction. *Aerosol Science and Technology* **1986**, *5*, 287–299.

3. Lecture 4 Ultrahigh Vacuum Science and ... - physics.uwo.ca http://www.physics.uwo.ca/~lgonchar/courses/p9826/Lecture4_UHV.pdf (accessed Jun 23, 2020).

4. Lecture 5 key ideas - New Jersey Institute of Technology https://web.njit.edu/~sosnowsk/Web659s11/Lecture%205%20key%20ideas.pdf (accessed Jun 23, 2020).

5. Vacuum, P. 1.2.5 Mean free path https://www.pfeiffer-vacuum.com/en/know-how/introduction-to-vacuum-technology/fundamentals/mean-free-path/ (accessed Jun 24, 2020).

6. https://cds.cern.ch/record/261730/files/p717.pdf (accessed Jun 24, 2020).

7. Scientific Overviews http://www.orsayphysics.com/what-is-uhv (accessed Jun 24, 2020).

8. Chrisey, D. B.; Pique, A.; Mcgill, R. A.; Horwitz, J. S.; Ringeisen, B. R.; Bubb, D. M.; Wu, P. K. Laser Deposition of Polymer and Biomaterial Films. *ChemInform* **2003**, *34*.

9. Kreutz, E. Pulsed Laser Deposition of Ceramics – Fundamentals and Applications. *Applied Surface Science* **1998**, *127-129*, 606–613.

10. Rao, M. C. Pulsed Laser Deposition — Ablation Mechanism And Applications. *International Journal of Modern Physics: Conference Series* **2013**, *22*, 355–360.

11. Yang, Z.; Hao, J. Progress in Pulsed Laser Deposited Two-Dimensional Layered Materials for Device Applications. *Journal of Materials Chemistry C* **2016**, *4*, 8859–8878.

12. Yao, J.; Zheng, Z.; Yang, G. Production of Large-Area 2D Materials for High-Performance Photodetectors by Pulsed-Laser Deposition. *Progress in Materials Science* **2019**, *106*, 100573.

13. A Simple Overview of Pulsed Laser Deposition (PLD) - Andor Learning Centre https://andor.oxinst.com/learning/view/article/pulsed-laser-deposition (accessed Jun 24, 2020).

14. Lowndes, D. H.; Geohegan, D. B.; Puretzky, A. A.; Norton, D. P.; Rouleau, C. M. Synthesis of Novel Thin-Film Materials by Pulsed Laser Deposition. *Science* **1996**, *273*, 898–903.

15. Popescu, C.; Dorcioman, G.; Popescu, A. C. Laser Ablation Applied for Synthesis of Thin Films: Insights into Laser Deposition Methods. *Applications of Laser Ablation - Thin Film Deposition, Nanomaterial Synthesis and Surface Modification* **2016**.

16. Kuppusami, P.; Raghunathan, V. S. Status of Pulsed Laser Deposition: Challenges and Opportunities. *Surface Engineering* **2006**, *22*, 81–83.

17. Zhang, Q.; Sando, D.; Nagarajan, V. Chemical Route Derived Bismuth Ferrite Thin Films and Nanomaterials. *Journal of Materials Chemistry C* **2016**, *4*, 4092–4124.

18. What are the differences between epitaxy, CVD and ALD? https://www.quora.com/What-are-the-differences-between-epitaxy-CVD-and-ALD (accessed Jun 24, 2020).

19. Saketi, S.; Olsson, M. Influence of CVD and PVD Coating Micro Topography on the Initial Material Transfer of 316L Stainless Steel in Sliding Contacts – A Laboratory Study. *Wear* **2017**, *388-389*, 29–38.

20. Higgins, M. Chemical Vapor Deposition Explained. Its Benefits and Drawbacks https://www.silcotek.com/semi-coating-blog/chemical-vapor-deposition-explained.-its-benefits-and-drawbacks (accessed Jun 24, 2020).

21. Smith, B. The Difference Between Physical Vapor Deposition (PVD) & Chemical Vapor Deposition (CVD) https://www.azom.com/article.aspx?ArticleID=17130 (accessed Jun 24, 2020).

22. Yoshitake, T.; Shiraishi, G.; Nagayama, K. Elimination of Droplets Using a Vane Velocity Filter for Pulsed Laser Ablation of FeSi2. *Applied Surface Science* **2002**, *197-198*, 379–383.

23. Boffa, V.; Petrisor, T.; Ciontea, L.; Gambardella, U.; Barbanera, S. High-Quality Surface YBCO Thin Films Prepared by off-Axis Pulsed Laser Deposition Technique. *Physica C: Superconductivity* **1997**, *276*, 218–224.

24. György, E.; Mihailescu, I.; Kompitsas, M.; Giannoudakos, A. Deposition of Particulate-Free Thin Films by Two Synchronised Laser Sources: Effects of Ambient Gas Pressure and Laser Fluence. *Thin Solid Films* **2004**, *446*, 178–183.

25. Ishihara, S.; Hanabusa, M. Laser-Assisted Chemical Vapor Deposition of Titanium Nitride Films. *Journal of Applied Physics* **1998**, *84*, 596–599.

26. Goto, T.; Kimura, T.; Tu, R. High-Speed Engineering Ceramic Coating by Laser Chemical Vapor Deposition. *Ceramic Transactions Series Ceramic Materials and Components for Energy and Environmental Applications* **2010**, 363–369.

27. Fang, Q.; Zhang, J.; Wang, Z.; He, G.; Yu, J.; Boyd, I. W. High-k Dielectrics by UV Photo-Assisted Chemical Vapour Deposition. *Microelectronic Engineering* **2003**, *66*, 621–630.

28. Boyd, D. A.; Greengard, L.; Brongersma, M.; El-Naggar, M. Y.; Goodwin, D. G. Plasmon-Assisted Chemical Vapor Deposition. *Nano Letters* **2006**, *6*, 2592–2597.

29. Chemical vapor deposition https://www.wikiwand.com/en/Chemical_vapor_deposition (accessed Jun 24, 2020).

30. X-Ray diffractometer and its various component parts for X-Ray studies http://xrd.co/component-parts-x-ray-diffractometer/ (accessed Jun 24, 2020).

31. lo250@cam.ac.uk. The Scanning Electron Microscope https://www.eng-atoms.msm.cam.ac.uk/RoyalSocDemos/SEM (accessed Jun 24, 2020).

32. Nanakoudis, A. What is SEM? Scanning Electron Microscopy Explained https://www.thermofisher.com/blog/microscopy/what-is-sem-scanning-electron-microscopy-explained/ (accessed Jun 24, 2020).

33. Granite, S. by. What is Raman Spectroscopy?: Raman Spectroscopy Principle https://www.edinst.com/blog/what-is-raman-spectroscopy/ (accessed Jun 24, 2020).

34. Burgens, L. The Atomic Force Microscopic (AFM) Characterization of Nanomaterials. **2009**.

35. Sponsored by Bruker Nano SurfacesFeb 21 2017. Using Non-Contact 3D Optical Profiling for Comprehensive Wafer Inspection https://www.azom.com/article.aspx?ArticleID=13598 (accessed Jun 24, 2020).

36. https://www.asminternational.org/documents/10192/1917570/htp00904p12.pdf/06d8f8e3-7320-451c-bd06-370be16df645 (accessed Jun 24, 2020).

37. https://www.researchgate.net/post/XRD_for_Si_100 (accessed Jun 24, 2020).

38. Scherrer equation https://en.wikipedia.org/wiki/Scherrer_equation (accessed Jun 24, 2020).

39. Khan, S.; Shahid, M.; Mahmood, A.; Shah, A.; Ahmed, I.; Mehmood, M.; Aziz, U.; Raza, Q.; Alam, M. Texture of the Nano-Crystalline AlN Thin Films and the Growth Conditions

in DC Magnetron Sputtering. *Progress in Natural Science: Materials International* **2015**, *25*, 282–290.

40. Qian, Y.; Shang, F.; Wan, Q.; Yan, Y. The Mechanism of Plastic Deformation in Intact and Irradiated GaN during Indentation: A Molecular Dynamics Study. *Computational Materials Science* **2018**, *149*, 230–242.

41. Zhang, J.; Cheng, H.; Chen, Y.; Uddin, A.; Yuan, S.; Geng, S.; Zhang, S. Growth of AlN Films on Si (100) and Si (111) Substrates by Reactive Magnetron Sputtering. *Surface and Coatings Technology* **2005**, *198*, 68–73.

42. http://prism.mit.edu/xray/oldsite/Introduction%20to%20HRXRD.pdf (accessed Jun 24, 2020).

43. Auner, G. W.; Jin, F.; Naik, V. M.; Naik, R. Microstructure of Low Temperature Grown AlN Thin Films on Si(111). *Journal of Applied Physics* **1999**, *85*, 7879–7883.

44. Smijesh, N.; Chandrasekharan, K.; Joshi, J. C.; Philip, R. Time of Flight Emission Spectroscopy of Laser Produced Nickel Plasma: Short-Pulse and Ultrafast Excitations. *Journal of Applied Physics* **2014**, *116*, 013301.

45. Uehara, K.; Aota, Y.; Shibata, T.; Kameda, S.; Nakase, H.; Isota, Y.; Tsubouchi, K. Surface Acoustic Wave Properties of Atomically Flat-Surface Aluminum Nitride Epitaxial Film on Sapphire. *Japanese Journal of Applied Physics* **2005**, *44*, 4512–4515.

46. Zhang, H.; Pelt, T. V.; Mehta, A. N.; Bender, H.; Radu, I.; Caymax, M.; Vandervorst, W.; Delabie, A. Nucleation and Growth Mechanism of 2D SnS 2 by Chemical Vapor Deposition: Initial 3D Growth Followed by 2D Lateral Growth. *2D Materials* **2018**, *5*, 035006.

47. Stranski–Krastanov growth https://en.wikipedia.org/wiki/Stranski%E2%80%93Krastanov_growth (accessed Jun 24, 2020).

48. Ambartsumov, M.; Tarala, V.; Krandievsky, S.; Kravtsov, A.; Sautiev, A.; Mitrofanenko, L. The Dependence of Aluminum Nitride Thin-Film Microstructure on the Number of Low-Temperature Plasma-Enhanced Atomic Layer Deposition Process Cycles. *Surface and Coatings Technology* **2019**, *378*, 124744.

49. Kallel, T.; Dammak, M.; Wang, J.; Jadwisienczak, W. Raman Characterization and Stress Analysis of AlN:Er3+ Epilayers Grown on Sapphire and Silicon Substrates. *Materials Science and Engineering: B* **2014**, *187*, 46–52.

50. Darakchieva, V.; Birch, J.; Schubert, M.; Paskova, T.; Tungasmita, S.; Wagner, G.; Kasic, A.; Monemar, B. Strain-Related Structural and Vibrational Properties of Thin EpitaxialAlNlayers. *Physical Review B* **2004**, *70*.